Determination of Characteristic Transport Coefficients of Porous Media from Volumetric Images using the Diffuse Interface Method

by

Chahat Aggarwal

A thesis

presented to the University of Waterloo

in fulfilment of the

thesis requirement for the degree of

Master of Applied Science

in

Chemical Engineering

Waterloo, Ontario, Canada, 2021

AUTHOR'S DECLARATION

I hereby declare that I am the sole author of this thesis. This is a true copy of the thesis, including any required final revisions, as accepted by my examiners.

I understand that my thesis may be made electronically available to the public.

ABSTRACT

Transport in engineered materials such as electrodes, membranes, filters, and natural materials such as rock, sand, soil can be modelled as transport in porous media. Direct Numerical Simulations (DNS) on volumetric images of porous media are commonly done using the Lattice Boltzmann Method (LBM), but this presents various challenges such as long computational time required to reach steady state, fixed grid coarseness, and limited availability of reliable LBM software, commercial or otherwise. Traditional finite element-based methods require conformal meshes of porous domains that are able to accurately capture fluid/solid interfaces, but at the cost of significant computational complexity and user-interaction in order to create the mesh.

To address these challenges, this work presents the application of a diffuse-interface finite element method that approximates a phase-field from volumetric images of porous media without user interaction and enables the use of a simple structured grid/mesh for traditional finite element-based fluid mechanics methods. The presented diffuse interface method (DIM) is automated and non-iterative, enabling the direct calculation of three characteristic coefficients from an input images: tortuosity, permeability, and inertial constant by simulating Fickian mass diffusion and single component incompressible Navier Stokes equation from low to high range of inlet velocity. Three different 2D test images with varying porosities are used to demonstrate the use of DIM. The method is compared to traditional FEM implementation using conformal meshes with respect to the agreement with determination of the characteristic coefficients, numerical accuracy, and computational requirements (time). Different parameters affecting accuracy of DIM were identified and ideal parameters were determined. At ideal parameters, relative error in tortuosity less than 0.75%, relative error in permeability less than 1% and relative error in inertial constant less than 3% was achieved for all three images. Though, DIM was found to be slower than traditional FEM implementation calling for optimized solvers for fluid flow on structured meshes to speed up the DIM simulations. The developed method provides an automated approach for computing effective transport properties from volumetric images of porous media.

ACKNOWLEDGEMENTS

DEDICATION

Dedicated to the most important people in my life- my parents, my brother, and my partner Gauri.

Table of Contents

LIST OF FIGURES

LIST OF TABLES

1 INTRODUCTION

1.1 Research Motivation

A porous material or porous medium is essentially a solid matrix containing voids usually called pores [1]. Fluid flow through porous medium is important to many fields such as purification, filtration, engineering (chemical engineering, petroleum engineering, bioremediation, construction engineering), geosciences (hydrogeology, petroleum geology, geophysics), biology, material science. Applications include estimates of subsurface contamination, geological CO_2 storage, explosivity of volcanic eruptions [2]–[4], energy conversion and energy storage devices, where porous electrode materials are essential for supercapacitors, fuel cells, and batteries [5].

Porosity, tortuosity, and permeability are central parameters for describing and understanding transport through the porous media. Porosity describes the volume fraction of voids in the medium. Tortuosity is a measure of effective transport length of particles transporting through the medium[6]. Permeability describes the ability of the medium to transport fluid due to a pressure gradient[7]. To determine these properties, experimentation needs to be done on each individual material under varying conditions which can be expensive and/or time consuming. Experiments involve applying boundary conditions that match the physical law being used and determining the fitting parameters for empirical relations. It can be difficult to determine the parameters accurately and experiments also require costly sensors. Experiments also involve physical activities which may be hazardous, risky and generate waste, especially when the experiment fails or if the assumptions are wrong. Hence, computational simulations become important to determine properties of porous media. They provide fast and inexpensive alternative to physical experiments. In addition, simulations help to assess and analyse pore scale phenomenon information as well which is often not observable by physical experiments such as pore size distribution and local transport phenomenon fields (concentration, velocity, pressure, temperature, etc.) [8].

Multiphysics simulations on images of porous media can be rather challenging due to unstructured, complex geometry and sharp interfaces. Complexity originates from meshing the geometry conformally meaning that the mesh must conform to cubic facets of porous media voxel image which often do not create smooth mesh surfaces since the actual surface of solid matrix in porous media is irregular. Apart from accurately conforming to solid boundaries of porous media, mesh should also be numerically stable and accurate. Methods have been published to automate the conformal mesh generation accurately for two- or three- dimensional domains [9] but the resulting numerical stability and accuracy of the simulation typically involves user-input, and generating conformal mesh is computationally expensive too.

To address the issues caused by meshing porous media geometry conformally, this work is based on implementing diffuse interface method (DIM) on images of porous media to simulate mass diffusion and fluid flow on a structured mesh over whole domain of interest. The diffuse interface method is a variation of immersed boundary method with a scalar phase field marking the different phases in domain[10], [11]. The phase field varies smoothly at the solid-fluid interface which is the key using non-conformal meshes. Diffuse interface methods with both uniform structured and adaptively refined meshes have been reported in the literature to mesh complex domains from volumetric images and perform fluid simulations [10]–[14]. This method allows a reduction in complexity associated with conformally meshing porous domains and to considerably reduce the number of mesh elements required to estimate pore space mass transport and fluid flow properties.

Past works from Nguyen et al, Stoter et al and Aland et al [10], [13], [15] demonstrated application of diffuse interface method on volumetric images using adaptively refined mesh for the phase-field on the solid-fluid interface region and a uniform mesh for the representation of the physics-based solution fields. Adaptively refining the mesh at solid-fluid interface adds extra complexity to the method and increases number of mesh elements. Porous media geometries have high surface area and irregulars features at interface which makes adaptive mesh refining unsuitable. This work implements a

2

uniform structured meshing for diffuse interface method and to generate the scalar phase field. Different parameters are identified and analysed which affect the accuracy of diffuse interface method and optimised to reach acceptable accuracy. The simulations are run using OpenCMP– an open source computational Multiphysics package [16] to determine characteristic properties of mass transport and fluid flow in porous media- tortuosity, permeability and inertial constant. The results from uniformly meshed diffuse interface method are then compared to results from traditional finite element method on conformal mesh to determine accuracy.

In summary, the diffuse interface method was analysed, and ideal parameters are predicted for structured uniform mesh of porous media domain to determine characteristic properties of fluid flow in porous media while reducing meshing complexity and reaching acceptable accuracy as compared to conformal meshing.

1.2 Objectives

The overall objective of this work was to implement the diffuse interface method on uniform structured meshes generated from volumetric images of porous media and determine characteristic coefficients from mass diffusion and incompressible Navier Stokes simulations. The specific steps taken are stated as follows-

- Generate uniform structured mesh of phase field from binary images of porous media.
- Determine suitable initial and boundary conditions for Poisson and incompressible Navier Stokes equations.
- Take existing implementation of diffuse interface method for Poisson equation and incompressible Navier Stokes equation, analyse and determine the ideal parameters that affect accuracy.
- Apply isomorphic transformation for Dirichlet boundary conditions at solid-fluid interface to prevent 'swelling' of solids.
- Constraint the diffuse interface width parameter to reduce degrees of freedom.

- Determine characteristic coefficients from diffuse interface method and measure accuracy as compared to finite element method simulations on conformal mesh.

1.3 Structure of Thesis

The thesis is distributed into following chapters: Chapter 1- Introduction, Chapter 2- Background and Literature Review, Chapter 3- Methodology, Chapter 0- Results and Discussions and Chapter 5- Conclusions and Recommendations.

Chapter 2 contains background on transport phenomenon in porous media and important properties, background and literature review on DNS methods used to determine properties, the finite element method with mathematics of weak formulation of relevant equations and lastly background and literature review on diffuse interface method and weak formulation of same relevant equations.

Chapter 3 discusses the methodology starting with obtaining the image, meshing-conformal and structured phase field, diffuse interface method parameters, formulation of the necessary equations with boundary conditions, solver settings and lastly generation of reference results for the same geometry on conformal meshes.

Chapter 4 presents the results and discussion starting with determination of tortuosity by diffuse interface method. Then a comprehensive comparison of tortuosity by two methods at varying DIM parameters is presented. Similar section follows on the determination of permeability and inertial constant by diffuse interface method, introducing isomorphic transformation to mitigate spheres swelling, optimising DI width based on isomorphic transformation and mesh coarseness. Then a comprehensive comparison of permeability and Forchheimer constant by two methods at varying DIM parameters is presented.

Chapter 5 summarizes conclusions from the work and recommend possible future work to improve the performance.

2 BACKGROUND AND LITERATURE REVIEW

2.1 Transport Phenomenon in Porous Media

Porous media can be defined as any material that contains a solid structure or matrix and open void spaces. The solid matrix can be deformable like a sponge or immobile solid like a piece of rock. There is no distinct degree of deformability of the solid matrix but the velocity of the solid phase with respect to the boundary of the system should be much less than the velocity of the fluid that can flow within the porous medium[17]. One additional requirement for a system to be considered as a porous medium would be accessibility of interconnected void spaces inside of solid matrix for fluid to flow. These void spaces are termed as pores. This work focuses entirely on single component mass and fluid flow through rigid solid matrix.

Porous media can be classified based on occurrence- natural versus artificial (example- Berea sandstone is naturally occurring, and ceramic material is man-made), on basis of permeability, on basis of consolidation (example- unconsolidated loose solid grains under gravity or pressure versus consolidated solid grains) and on basis of size range of pores. The size ranges can vary anywhere between $1\ nm$ to $1\ mm$. The International Union of Pure and Applied Chemistry (IUPAC) classified porous media for chemists based on pore sizes, R_p as follows-

- Macroporous: $R_p > 150\ nm$
- Mesoporous: $5\ nm < R_p < 150\ nm$
- Microporous: $R_p < 5\ nm$

Since IUPAC classifies a relatively short range of R_p sizes, engineers generally use the term nano porous for pore sizes $R_p < 1000\ nm$.

To overcome difficulty posed by physical experiments, volumetric images of porous media are used by researchers to conduct image analysis[18], [19] and determine

properties by numerical simulations [20]. These images are basically two- or three-dimensional arrays and can be either greyscale or binary. Grayscale images are arrays with values between 0 and $2^{nbits} - 1$ where $nbits$ is the number of bits in a byte or, more simply put, it is the numerical accuracy of the image. The typical digitization process of an image, stores images with 8 bits per byte. Thus, giving a range of values from 0 to 255 where 0 is black, 255 is white and intermediate values are Gray with increasing brightness from 0 to 255. Binary images have elements with values of either 0 or 1. The value of each element in a binary array indicates the phase. There are number of ways to experimentally obtain volumetric images of porous media such as-

- Serial Sectioning
- Tomography
- Magnetic Resonance Imaging (MRI)

Though, these methods give exact images of geometrical and mineralogical morphology of the pore space, only a single image of the investigated porous material sample is typically acquired. Due to variability associated with the morphology of porous material, often numerous images of the same porous material type are required to obtain a distribution over larger volume. Experimental acquisition of these high-resolution images by above mentioned methods is time consuming and expensive. Artificial generation of images enable customization and save resources used on actual imaging without having a real sample image. Figure 1 presents an example of artificial 2D image with colour 'black' representing solid domain and 'white' representing pore space. This work artificially generates and uses 2D binary images as a representation of porous media with 1 representing pore space and 0 representing solid domain.
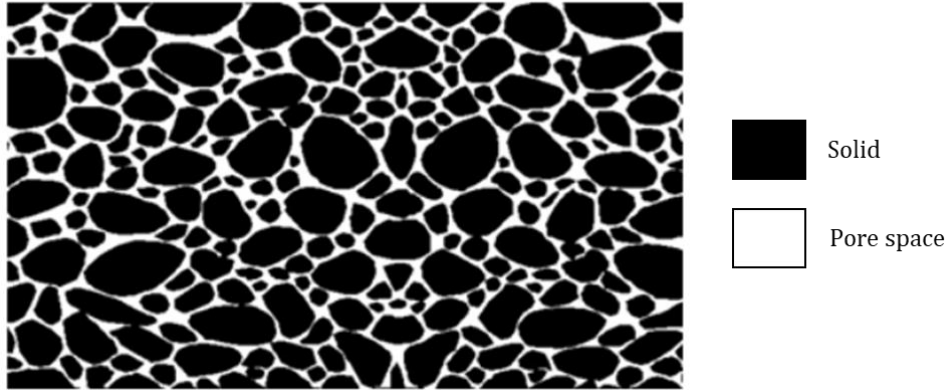
Figure 1: Artificial 2D binary image representing microscopic cross section of a Porous Material

The following sections give a background and literature review on the characteristic properties of porous media-

2.1.1 Porosity

One of the most important parameters to determine fluid flow properties through porous media is the measure of open space inside solid matrix that facilitate transport of mass and fluid across the medium [21]. The open space inside solid matrix is known as pores and this property is termed as porosity (ε). Porosity is the ratio of the pore volume to the total volume (bulk volume) given by equation (2.1):

$$\varepsilon = \frac{V_p}{V_p + V_s} = 1 - \frac{V_s}{V_b} \tag{2.1}$$

where, V_p is volume occupied by pores, V_s is volume occupied by pores and V_b is the bulk volume. $V_b = V_s + V_p$

It is commonly observable for some pores to get trapped inside solid matrix and become isolated from other pores. A porous material sample might have large porosity but no conductivity of fluid because of no interconnection. Transportation of fluids through porous medium is thus controlled by connected pores. These trapped pores reduce the overall effective porosity. Hence, two different types of porosities are defined-

- Absolute Porosity (ε_a)- The ratio of the total pore space in the porous medium to that of the bulk volume.

$$\varepsilon_a = \frac{V_{p_{Total}}}{V_{p_{Total}} + V_s} = 1 - \frac{V_s}{V_b} \qquad \textbf{(2.2)}$$

- Effective Porosity (ε_{eff})- The ratio of the interconnected pore space in the porous medium to that of the bulk volume. For most practical and engineering purposes, effective porosity is used.

$$\varepsilon_{eff} = \frac{V_{p_{eff}}}{V_b} \qquad \textbf{(2.3)}$$

2.1.2 Tortuosity

In addition to the amount of void space available for transport, other important factor is the connectivity of pores inside solid matrix. The disordered nature of the pore structures result in a "tortuous" internal flow path for fluid permeation, molecular diffusion, electrical conduction, and heat transfer [22]–[30]. In geology, tortuosity affects parameters such as permeability, effective diffusivity, formation resistivity factor, and thermal conductivity [6], [28]–[31]. Tortuosity is a significant component in the design of electrodes for energy storage and conversion to increase battery capacity [32]–[34], in chemical catalysis for reaction efficiency [35], in water treatment for distillation performance [36] and in bone tissue engineering by affecting cell migration [37]. Due to variety of applications in various fields, tortuosity, unlike other standard pore structure properties, is vaguely defined with several definitions and evaluation methods used in different models and situations. Geometrical tortuosity can be used to characterize the morphological property of pore structures, while physical tortuosities - hydraulic, electrical, diffusional, and thermal tortuosities can be defined to describe different transport processes in porous media [28]. Geometrical and physical tortuosities are described in detail as follows-

8

GEOMETRICAL TORTUOSITY

The ratio of effective flow path length (L_H) to straight line distance L in the macroscopic flow direction is defined as geometrical tortuosity (τ_g) [27], [38]. Geometrical tortuosity is a pore structure property that is solely determined by the geometrical and morphological characteristics of porous media. There are many image analysis-based algorithms which can be used to determine the shortest connected path between two opposite surface pixels/voxels on one side of the digital pore structure and another surface pixel/voxel on the other. Some of these methods are the direct shortest-path search method (DSPSM), the skeleton shortest path search method (SSPSM), the fast marching method (FMM), the pore centroid method (PCM), etc. [28]. These image-based algorithms work directly with pixel/voxel data, and they're usually simple to build and fast to compute. It's worth noting, however, that geometrical tortuosity does not account for pore radius change along pore channels, even though the narrowing and hindrance of pore structures play an important role in transport qualities.

$$\tau_g = \frac{L_H}{L} \tag{2.4}$$
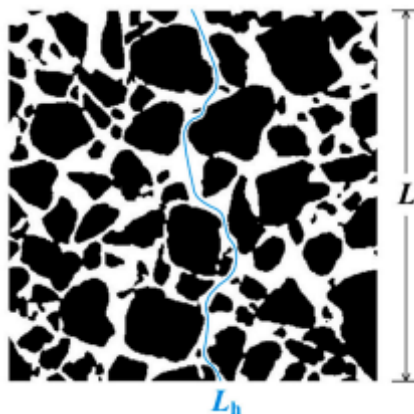
Figure 2: Effective flow-path length L_h and straight-line distance L in a 2D digital microstructure

PHYSICAL TORTUOSITY

The estimation of tortuosity from pore scale transport phenomenon is termed as physical tortuosity. These transport phenomena can be fluid flow, electric conduction, molecular diffusion, and heat transfer and are governed by two principles at steady state [39]- (1) the conservation law which governs the conservation of physical quantity of transport matter (mass, charge, energy, momentum) and (2) the behaviour of transport matter within a control volume. The steady-state flux of different transport matter driven by an applied force can be used to determine physical tortuosities. Assuming the density of transport matter is constant and independent of space and time, the continuity equation can be stated as:

$$\boldsymbol{\nabla}.\boldsymbol{J} = 0 \qquad\qquad \textbf{(2.5)}$$

where $\boldsymbol{J}$ is the steady-state flux of transport matter. Various transport processes are governed by similar macroscopic laws (e.g., Darcy's, Fick's, Ohm's, Fourier's, and Newton's law), which have the following general expression [39]:

$$\boldsymbol{J} = -\delta \boldsymbol{\nabla} F_{drive} \qquad\qquad \textbf{(2.6)}$$

where the steady-state flux $\boldsymbol{J}$ of transport matter is proportional to the applied driving force ∇F_{drive}, and the proportionality constant δ is the phenomenological coefficient corresponding to transport property (i.e., intrinsic permeability, diffusion coefficient, electrical conductivity, thermal conductance, or dynamic viscosity).

The different transport phenomena that can be analysed based on equations (2.5) and (2.6) are presented in Table 1 as following –

Table 1: Different transport phenomena in porous media

Transport Phenomena	Driving Force	Governing relationship	Proportionality constant	Definitive Law
Molecular diffusion	Concentration gradient	$J_d = -D\boldsymbol{\nabla}C$	Diffusion coefficient D	Fick's law
Electric conduction	Voltage gradient	$J_e = -\sigma\boldsymbol{\nabla}V$	Electric conductivity σ	Ohm's law
Heat transfer	Temperature gradient	$J_h = -\lambda\boldsymbol{\nabla}T$	Thermal conductance λ	Fourier law
Fluid flow	Pressure Gradient	$J_v = -K\boldsymbol{\nabla}P$	Intrinsic permeability K	Darcy's law

where J_d, J_e, J_h, J_v represent diffusion flux, electric charge flux, heat flux and volumetric fluid flux respectively.

The tortuosity of a porous medium determined by concentration flux within porous media of diffusing gases is known as diffusional tortuosity. This work focuses on determination of diffusional tortuosity. The effective diffusivity of a gas within porous media D_{eff} is observed to be lower than the diffusing gas's bulk diffusivity D_0. Diffusional tortuosity explains the lower diffusivity by relating the effect of morphology on diffusive flux and is given by [40], [41]:

$$\tau = \frac{D_0}{D_{eff}}\varepsilon \tag{2.7}$$

The steady state diffusive flux passing through porous media is compared against steady state diffusive flux of similar gas through a homogenous open space with similar dimensions. The ratio of both fluxes gives diffusional tortuosity. Fick's law can be used to calculate the diffusional flux travelling through porous media and the homogeneous open space:

$$J_d^{pore} = -AD_{eff}\nabla C \qquad\qquad\qquad \textbf{(2.8)}$$

$$J_d^{free} = -AD_0\nabla C \qquad\qquad\qquad \textbf{(2.9)}$$

where J_d^{pore} and J_d^{free} are diffusional fluxes travelling through porous media and the homogeneous open space respectively. By substituting equation (2.8) and (2.9) into equation (2.7), diffusional tortuosity τ_d is given as:

$$\tau_d = \frac{D_0}{D_{eff}}\varepsilon = \frac{J_d^{free}}{J_d^{pore}}\varepsilon \qquad\qquad\qquad \textbf{(2.10)}$$

2.1.3 Permeability and Forchheimer Constant

The early research to model fluid flow through porous media started with observations and experiments to describe the bulk behaviour of porous media [42]. Because the system's fundamental equation, the Navier-Stokes equation, and the physical structure of porous media were too complex for researchers to derive a mathematical model, many researchers relied on experiment and observation to comprehend porous media[43]. The Darcy model is one of the most widely used models for estimating flow across porous media. Henry Darcy was the first to develop the model in 1856 [42]. Darcy undertook a series of tests on subsurface fluid flow and water supply using water flowing down a column of packed sand. Darcy was able to deduce from this experiment that the pressure differential in the column was linearly related to velocity.

$$-\nabla p = \boldsymbol{a} \cdot \boldsymbol{V} \qquad\qquad\qquad \textbf{(2.11)}$$

where p represents pressure, $\boldsymbol{a}$ represents Darcy coefficient and $\boldsymbol{V}$ represents velocity.

The Darcy coefficient is a vector for any porous media since it depends on the direction of fluid flow. It can be defined for a single direction as:

$$a = \frac{\mu}{K} \qquad\qquad\qquad \textbf{(2.12)}$$

where μ is fluid viscosity and K is the porous media permeability.
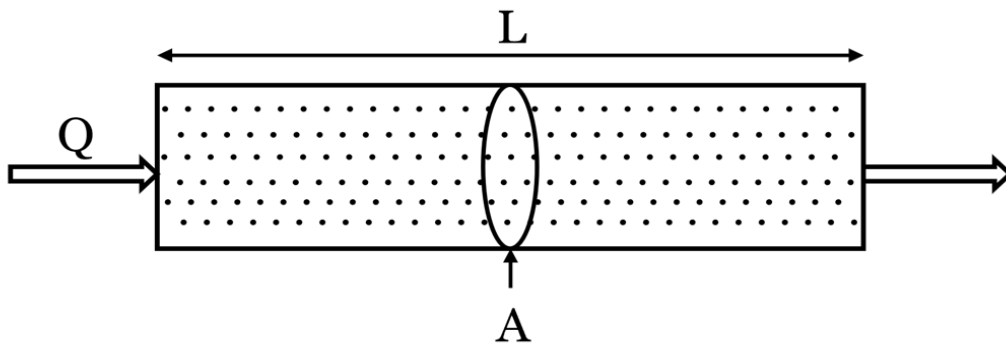
Figure 3: Representation of flow through porous media with cross-section area A, length L and flowrate Q. The flux of fluid flow is Q/A with pressure gradient applied between inlet and outlet.

Henry Darcy was only able to examine low flow rates in his tests due to the technological limitations at the time. Forchheimer in 1901 repeated Darcy's experiments and determined that the equation (2.11) only holds true for low flow rates (Re < 10) [44]. It was observed that at higher flowrates, the inertial forces arising from variations in flow velocity or direction along the flow paths due to constrictions or obstructions had significant effects on pressure drop resulting in an additional quadratic term between the pressure gradient and the velocity. Thus, Forchheimer added a second term to Darcy's model [45], which changes equation (2.11) to:

$$-\nabla p = \boldsymbol{a} \cdot \boldsymbol{V} + \boldsymbol{b} \cdot \boldsymbol{V}^2 \qquad\qquad\qquad \textbf{(2.13)}$$

where $\boldsymbol{b}$ represents Forchheimer coefficient. Forchheimer coefficient is a vector for any porous media since it depends on the direction of fluid flow. It can be defined for a single direction as:

$$b = \beta\rho \qquad\qquad\qquad \textbf{(2.14)}$$

where ρ is fluid density and β is non-Darcy coefficient or the inertial resistance. It is also established that coefficient a represents the intrinsic permeability of the porous media because of inverse relationship to permeability [46]–[48] whereas, coefficient b depends on the geometrical properties of porous media and needs to be determined by experiments or simulations [49], [50].

The observed pressure drop due to inertial forces can also be described by an analogous example of flow in a straight tube versus in a bent elbow. The presence of a radial pressure differential caused by the centrifugal force acting on the fluid is the most distinguishing feature of flow through a bend. As a result, the fluid in the pipe's centre flows to the outer edge and then back along the wall to the inner side. This results in a double spiral flow field, as shown in Figure 4. If the bent elbow curvature is strong enough, the pressure gradient at the outer wall in the bend and near the inner wall just after the bend may cause flow separation at these spots, resulting in a considerable increase in pressure losses. Friction and momentum exchanges generated by a change in flow direction are both responsible for pressure losses in a bend. Both of these variables are influenced by the bend angle, curvature ratio, and Reynolds number. The overall pressure drop can be expressed as the sum of two components: 1) friction in a straight pipe of equivalent length, which is primarily determined by the Reynolds number (and pipe roughness); and 2) losses due to direction change, which are typically expressed in terms of a bend-loss coefficient and are primarily determined by the curvature ratio and bend angle.
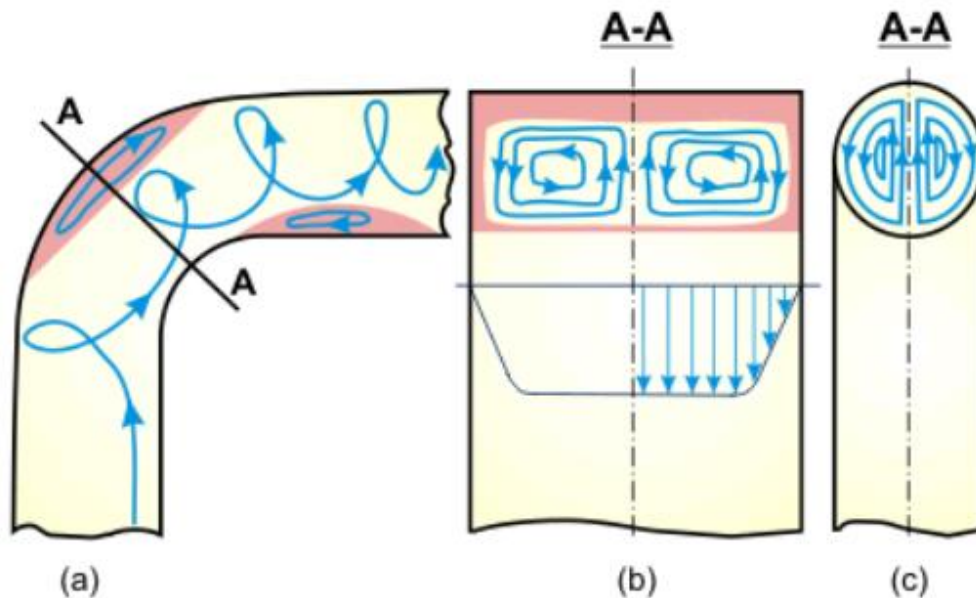
Figure 4: Schematic diagram of flow in an elbow; (a) longitudinal section; (b) rectangular cross-section; (c) circular cross-section [51]

Now, based on the Darcy and Forchheimer model, the flow in porous media can be categorised into two regimes- Darcy flow and non-Darcy flow as shown in Figure 5. Darcy flow is defined as a flow region in which the change in pressure is proportional to velocity, or a flow region in which Darcy's law, equation (2.11), applies to a porous material. The viscous stress in the fluid as it flows through the pore spaces controls Darcy flow. The zone in which fluid velocity is high for Darcy's law to apply is referred to as non-Darcy flow. In this region, in addition to the viscous forces that govern Darcy's law, the inertial effects of the flow through porous media become significant. When Reynolds number of fluid flow through porous domain is greater than 10, non-Darcy flow is said to exist, though this may vary system to system.
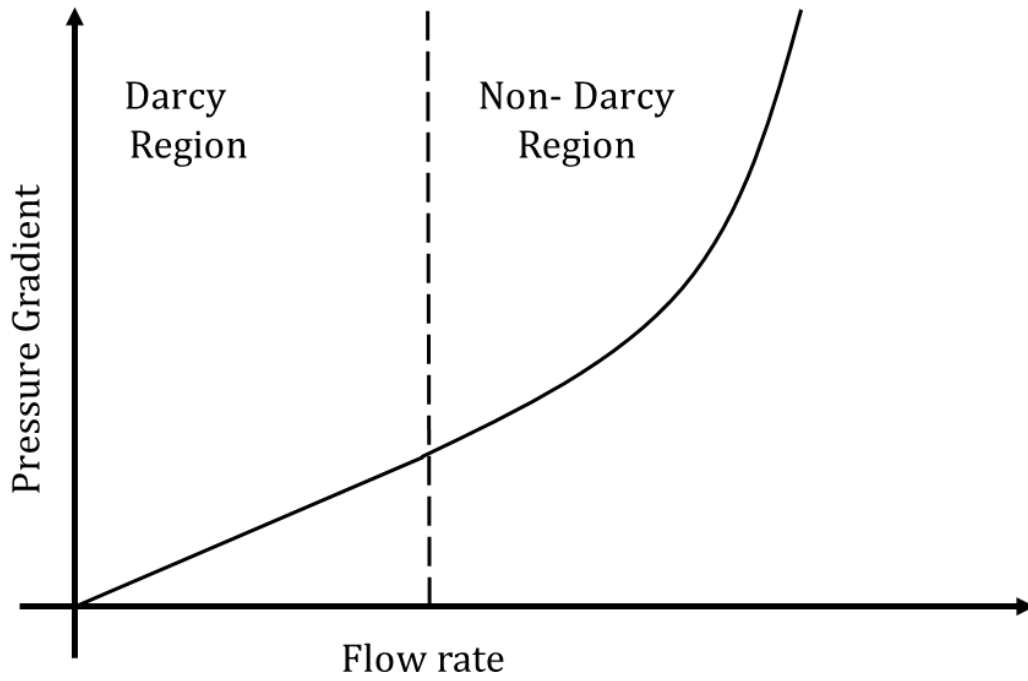
Figure 5: Representation of different flow regimes based on flow rate. Also called Darcy-Forchheimer Curve

2.2 Numerical methods for Pore Scale Resolution of Porous Media

Numerical methods for pore scale resolution of porous media refer to the use of the voxel image as the grid for computing fluid flow and mass transfer. This approach allows for the inclusion of pore structure directly in simulations, thereby accounting for the impact of the porous material. Numerical methods for pore scale simulations can be categorised on basis of spatial discretization techniques i.e., structured, and unstructured grid models. The structured method is used in the majority of grid-based pore-scale simulations. This popularity stems from the Lattice-Boltzmann method's success in simulating flows for complex geometries. The method also enables for the mesh generation stage to be bypassed by considering the volumetric image as a structured grid, which is significant.

Traditional numerical techniques such as finite difference, finite volume and finite element methods are also applicable to use on structured grids. However, structured grids are unsuitable for complex geometries such as porous media since the curved surfaces become stepped and jagged, which causes problems especially for higher velocity flow. Unstructured grids on the other hand are based on a connected collection of polyhedral, tetrahedral, hexahedral, or prism shaped grids to describe an unstructured representation of a particular computational domain. Despite widespread recognition that unstructured grids are well adapted to geometrically complex domains, only few investigations of flow in porous media have employed this method [52], [53] because of the complexity associated with generating unstructured meshes for porous media. Even with recent advancement in mesh generation techniques and improving high performance computing resources, unstructured grids are difficult to generate, time consuming and require advanced meshing tools such as GMSH [54], Avizo [55]and commercial Multiphysics modelling and simulation software such as COMSOL Multiphysics [56], ANSYS Fluent[57].

2.2.1 Lattice Boltzmann Method (LBM)

The Lattice Boltzmann Method (LBM) has been a popular method for simulating fluid flows in porous media. Unlike traditional approaches that explicitly discretize the continuum equations of transport when studying fluid flow, LBM uses kinetic theory to derive a discrete approximation to the incompressible Navier-Stokes equations. There are some advantages of using Lattice Boltzmann approach for pore-scale modelling [58]. A voxel or pixel image can be directly used as a structured grid for LBM. Due to the explicit character of the method, the use of local pointers/vectors, and a lattice-based distribution of particle sites well suited to domain decomposition, Lattice Boltzmann systems are by nature well adapted to parallelization. Furthermore, pressure is determined using an equation of state, eliminating the necessity to solve a pressure Poisson equation to resolve the incompressibility restriction.

However, Lattice Boltzmann Method comes with limitations as well. M. Goodarzi, M. R. Safaei et al. conducted a comprehensive comparison of the Lattice Boltzmann and finite volume methods for solving natural convection heat transfer problems inside cavities and enclosures using various discretization schemes and pressure-velocity linking algorithms [59]. The finite volume method results were found to be more accurate compared to those of LBM, especially at the corners and LBM required 4-5 times the CPU time and 8-9 times the iteration to solve the considered testcase. LBM is found to have problems with fluid flows with Mach numbers greater than 0.1 even at the expense of a compressibility error [60], [61]. Flows with pressure variations or density variations greater than 0.01 also show significant deviations from incompressible Navier-Stokes flows. Although, the Mach numbers and density fluctuations in pore scale flows are often minimal, the Mach numbers and density fluctuations in the lattice Boltzmann models used to mimic similar processes can be significantly greater.

2.2.2 Conventional Numerical Methods

Navier-Stokes equations are solved in conventional numerical methods by discretizing the spatial differential operators on a Eulerian grid using techniques like the finite difference method (FDM), finite volume method (FVM), or finite element method (FEM). If the computational grid is fine enough, all three approaches should produce the same result. In general, the rate of convergence of these numerical methods depend on the complexity and heterogeneity of the porous medium [62]. The finite difference approach approximates the derivatives of the differential equation in terms of solution values at neighbouring mesh nodes using a Taylor series expansion. On Euclidean grids, it is simple to apply and quite successful. When dealing with complex geometries, however, FDM can be challenging to apply [63]. The finite volume technique uses a zeroth-order approximation of the solution within each mesh element, which can vary discontinuously between mesh elements, making the method relatively stable. Flux balances over each mesh element and the continuity of fluxes between neighbouring mesh elements are used to determine the specific value of the approximate solution within each mesh element. This also makes the finite volume technique conservative locally. Though, the application of FVM to scenarios with complex changing boundaries is difficult and sophisticated [64]. The finite element approach uses higher-order polynomial interpolants within mesh elements to ensure that the approximate solution remains consistent across mesh element nodes without imposing flow constraints. In comparison to the finite volume method, this enhances accuracy at the expense of stability and local conservation [65],[66]. Though, many new advances made to the finite element method address the main issues. This work is focused on using FEM for porous media on an unstructured conformal and a structured grid separately. FEM is discussed in more detail in section 2.3 and mathematical weak forms for the concerned equations are formulated for the model.

2.3 Finite Element Method

The finite element method (FEM) has been a popular method for solving differential equations. FEM allows a wide range of differential equations from many scientific applications to be analysed and solved within a similar framework. This is owing to the fact that it is derived in a very general way using a weak formulation of a physical problem. Furthermore, improving the numerical method's order simply by changing the basis functions is quite useful. The FEM can be derived from method of weighted residuals [67]. The space is partitioned into connected elements for the finite element method. Piecewise polynomial functions are used to approximate the solution in each of these elements. For each nodal point, a collection of basis functions is defined. After that, they can be used to estimate derivatives. For example, piecewise linear basis functions are presented in Figure 6. Higher-order basis functions can also be generated. These can be used to improve the solution's accuracy. Each element, however, will require the addition of another node.
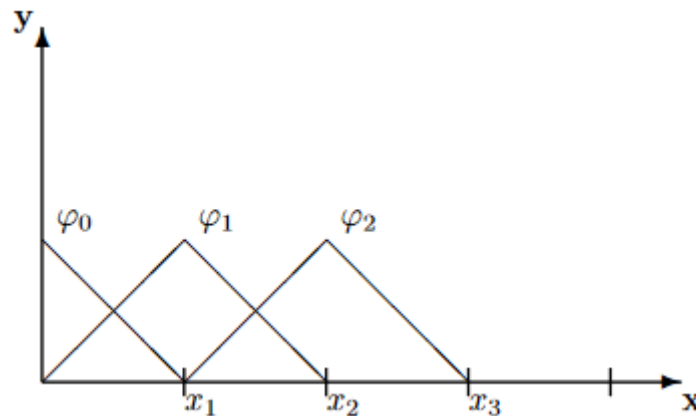
Figure 6: Example of finite element method's piecewise linear basis functions.

While the finite element method has been widely utilised to solve fluid flow issues, it has only been applied to flow in porous medium in a limited number of cases. The finite element method works well with unstructured tetrahedral grids. Simple 2D geometries

20

or simple 3D arrangements of spherical particles have been studied in certain significant research [68], [69]. These findings, on the other hand, have not been applied in a broad sense to challenges involving image-based pore-scale modelling. Section 2.3.1 and 2.3.2 present derivation of weak forms for Poisson and incompressible Navier Stokes equation respectively as needed for the project:

2.3.1 Poisson Equation

The following Poisson equation is presented, and weak form is derived:

$$- \nabla^2 u = f \ \text{ in } \ \Omega \qquad \qquad \textbf{(2.15)}$$

where u is an unknown function, f is a forcing function and Ω is the domain.

The following boundary conditions are applied:

$$u = g \ \text{ on } \partial\Omega_D \qquad \qquad \textbf{(2.16)}$$

$$-\boldsymbol{n}.\boldsymbol{\nabla} \, u = h \ \ on \ \partial\Omega_N \qquad \qquad \textbf{(2.17)}$$

$$-\boldsymbol{n}.\boldsymbol{\nabla} \, u = r(u - q) \ \ on \ \partial\Omega_R \qquad \qquad \textbf{(2.18)}$$

where $\partial\Omega_D, \partial\Omega_N$ and $\partial\Omega_R$ are Dirichlet, Neumann and Robin conditions respectively.

For weak formulation, the Poisson equation (2.15) is multiplied with a test function v and integrated:

$$- \int_\Omega (\nabla^2 u)v = \int_\Omega fv \ \text{ in } \ \Omega \qquad \qquad \textbf{(2.19)}$$

Now, we can expand the left-hand side of (2.19) by either product rule of differentiation or Divergence Theorem. Using product rule of differentiation on $\boldsymbol{\nabla}.v$:

$$\boldsymbol{\nabla}.(\boldsymbol{\nabla}\text{uv}) = (\nabla^2 u)v + (\boldsymbol{\nabla}u).(\boldsymbol{\nabla}v) \qquad \qquad \textbf{(2.20)}$$

$$-\int_{\Omega} (\nabla^2 u)v = \int_{\Omega} (\nabla u).(\nabla v) - \int_{\Omega} \boldsymbol{\nabla}.(\boldsymbol{\nabla} uv) \qquad (2.21)$$

Now, we can write $\int_{\Omega} \boldsymbol{\nabla}.(\boldsymbol{\nabla} uv)$ as:

$$\int_{\Omega} \boldsymbol{\nabla}.(\boldsymbol{\nabla} uv) = \int_{\partial\Omega} \left(\frac{\partial u}{\partial n}\right) v \qquad (2.22)$$

Substituting (2.22) back in (2.19):

$$\int_{\Omega} (\nabla u).(\nabla v) - \int_{\partial\Omega} \left(\frac{\partial u}{\partial n}\right) v = \int_{\Omega} fv \qquad (2.23)$$

A different space is defined for test function v such that $v = 0$ on $\partial\Omega_D$

Now, the Neumann and Robin boundary conditions can be substituted directly into (2.23) and considering test function v vanishes on Dirichlet boundary. We get a simplified weak form with all the boundary conditions inserted:

$$\int_{\Omega} (\nabla u).(\nabla v) - \int_{\partial\Omega_N} vh - \int_{\partial\Omega_R} vr(u-q) = \int_{\Omega} fv \qquad (2.24)$$

2.3.2 Incompressible Navier Stokes Equation

In order to find a weak form of the Navier-Stokes equations, firstly, we start with the momentum equation:

$$\frac{\partial \boldsymbol{u}}{\partial t} - \nu\nabla^2\boldsymbol{u} + (\boldsymbol{u} \cdot \boldsymbol{\nabla})\boldsymbol{u} + \nabla p = \boldsymbol{f} \text{ in } \Omega \qquad (2.25)$$

where ν is kinematic viscosity and $\boldsymbol{f}$ is some body force.

The following boundary conditions are considered:

$$\boldsymbol{u} = \boldsymbol{g} \text{ on } \partial\Omega_D \qquad (2.26)$$

$$-\boldsymbol{n}.(\nu\boldsymbol{\nabla}\,\boldsymbol{u}-p)=\boldsymbol{h}\;\; on\;\partial\Omega_N \tag{2.27}$$

$$-\boldsymbol{n}.(\nu\boldsymbol{\nabla}\,\boldsymbol{u}-p)=\boldsymbol{r}(\boldsymbol{u}-q)\;\; on\;\partial\Omega_R \tag{2.28}$$

The, multiply it with a test function v, defined in a suitable space V, and integrate both members with respect to the domain Ω :

$$\int_\Omega \frac{\partial \boldsymbol{u}}{\partial t}\cdot\boldsymbol{v}-\int_\Omega \nu\nabla^2\boldsymbol{u}\cdot\boldsymbol{v}+\int_\Omega(\boldsymbol{u}\cdot\boldsymbol{\nabla})\boldsymbol{u}\cdot\boldsymbol{v}+\int_\Omega\boldsymbol{\nabla}p\cdot\boldsymbol{v}=\int_\Omega\boldsymbol{f}\cdot\boldsymbol{v} \tag{2.29}$$

Counter-integrating by parts the diffusive and the pressure terms and by using the Gauss' theorem:

$$-\int_\Omega \nu\nabla^2\boldsymbol{u}\cdot\boldsymbol{v}=\int_\Omega \nu\boldsymbol{\nabla}\boldsymbol{u}\cdot\boldsymbol{\nabla}\boldsymbol{v}-\int_{\partial\Omega}\nu\frac{\partial\boldsymbol{u}}{\partial\mathbf{n}}\cdot\boldsymbol{v} \tag{2.30}$$

$$\int_\Omega \boldsymbol{\nabla}p\cdot\boldsymbol{v}=-\int_\Omega p\boldsymbol{\nabla}\cdot\boldsymbol{v}+\int_{\partial\Omega}p\boldsymbol{v}\cdot\boldsymbol{n} \tag{2.31}$$

Using these relations,

$$\int_\Omega \frac{\partial \boldsymbol{u}}{\partial t}\cdot\boldsymbol{v}+\int_\Omega \nu\boldsymbol{\nabla}\boldsymbol{u}\cdot\boldsymbol{\nabla}\boldsymbol{v}+\int_\Omega(\boldsymbol{u}\cdot\boldsymbol{\nabla})\boldsymbol{u}\cdot\boldsymbol{v}-\int_\Omega p\boldsymbol{\nabla}\cdot\boldsymbol{v}$$
$$=\int_\Omega\boldsymbol{f}\cdot\boldsymbol{v}+\int_{\partial\Omega}\left(\nu\frac{\partial\boldsymbol{u}}{\partial\boldsymbol{n}}-p\mathbf{n}\right)\cdot\boldsymbol{v} \tag{2.32}$$

Similarly, the continuity equation is multiplied by a test function q belonging to a test space Q and integrated in the domain Ω:

$$\int_\Omega q\boldsymbol{\nabla}.\boldsymbol{u}=0 \tag{2.33}$$

Considering that the test function v vanishes on the Dirichlet boundary $\partial\Omega_D$ and considering Neumann boundary condition on $\partial\Omega_N$, the integral on boundary can be rearranged as:

$$\int_{\partial\Omega}\left(v\frac{\partial\boldsymbol{u}}{\partial\mathbf{n}}-p\mathbf{n}\right)\cdot\boldsymbol{v}=\underbrace{\int_{\partial\Omega_D}\left(v\frac{\partial\boldsymbol{u}}{\partial\boldsymbol{n}}-p\mathbf{n}\right)\cdot\boldsymbol{v}}_{\boldsymbol{v}=0 \text{ on } \partial\Omega_D}+\int_{\partial\Omega_N}\underbrace{\left(v\frac{\partial\boldsymbol{u}}{\partial\mathbf{n}}-p\mathbf{n}\right)}_{=\boldsymbol{h} \text{ on } \partial\Omega_N}\cdot\boldsymbol{v}$$

$$+\int_{\partial\Omega_R}\underbrace{\left(v\frac{\partial\boldsymbol{u}}{\partial\mathbf{n}}-p\mathbf{n}\right)}_{=\boldsymbol{r}(\boldsymbol{u}-\boldsymbol{q}) \text{ on } \partial\Omega_R}\cdot\boldsymbol{v}=\int_{\partial\Omega_N}\boldsymbol{h}\cdot\boldsymbol{v}+\int_{\partial\Omega_R}\boldsymbol{r}(\boldsymbol{u}-\boldsymbol{q})\cdot\boldsymbol{v}$$

$$(2.34)$$

Having this in mind, the weak formulation of the Navier-Stokes equations is expressed as:

$$\int_{\Omega}\frac{\partial\boldsymbol{u}}{\partial t}\cdot\boldsymbol{v}+\int_{\Omega}v\boldsymbol{\nabla u}\cdot\boldsymbol{\nabla v}+\int_{\Omega}(\boldsymbol{u}\cdot\boldsymbol{\nabla})\boldsymbol{u}\cdot\boldsymbol{v}-\int_{\Omega}p\boldsymbol{\nabla}\cdot\boldsymbol{v}$$

$$=\int_{\Omega}\boldsymbol{f}\cdot\boldsymbol{v}+\int_{\partial\Omega_N}\boldsymbol{h}\cdot\boldsymbol{v}+\int_{\partial\Omega_R}\boldsymbol{r}(\boldsymbol{u}-q)\cdot\boldsymbol{v} \; for \; \boldsymbol{v}\in V$$

$$(2.35)$$

$$\int_{\Omega}q\boldsymbol{\nabla}\cdot\boldsymbol{u}=0 \; for \; q\in Q$$

$$(2.36)$$

2.4 Diffuse Interface Method

Traditional finite element method implementation is based on a simulation domain represented by a mesh conforming to the shape of the domain. The mesh nodes lie on the domain boundary, but the mesh edges do not. Sufficient mesh refinement is needed to correctly approximate the surface boundary. Figure 7 shows increasing levels of mesh refinement to accurately conform to the simulation domain. The mesh refinement can get increasingly tedious for geometries with irregular features and high curvatures such as porous media.

(a)   (b)   (c)   (d)
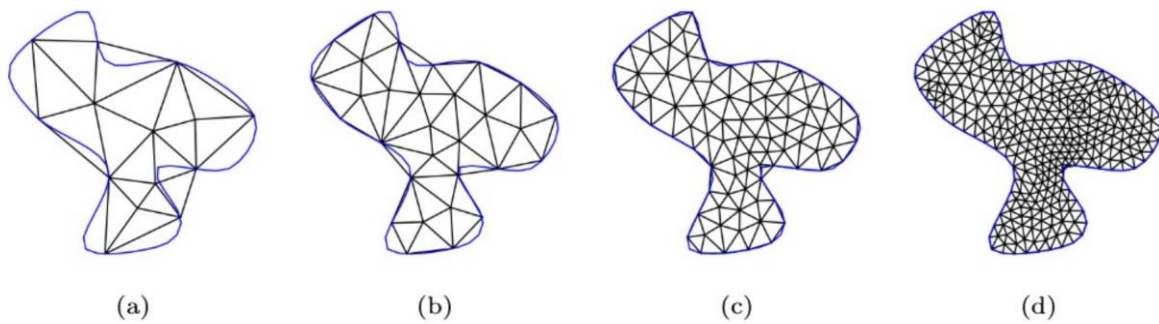
Figure 7: Example of complex geometry meshed conformally with increasing refinement level with unstructured triangular mesh. This figure was taken from Monte et al [11].

Since porous media geometries are difficult to conformally mesh with structured and/or quadrilateral/hexahedral meshes, unstructured triangular or tetrahedral meshes are often utilised [70]. This, however, ignores the several advantages of structured quadrilateral/hexahedral meshes. Structured meshes are easier and less memory intensive to store than unstructured meshes since they have simple connectivity architectures. Because organised meshes provide easy-to-solve sparse matrices with non-zero entries confined to the main diagonal or more diagonals on either side, simulations are less computationally intensive. Furthermore, structured meshes are well-suited to GPU acceleration [71]. When aligned with the dynamics of the solution field, such as the direction of flow in fluid dynamics simulations, quadrilateral/hexahedral mesh elements improve simulation stability and numerical accuracy. They can also be extended in this direction without losing their shape, allowing

for coarser meshes without reducing mesh quality [72]. Additionally, building unstructured conformal meshes for complex geometry such as porous media is difficult and time consuming. Typical approach of the meshing process involves CAD-based (Computer Aided Design) meshing. Any given domain must first be characterised by a surface in the CAD-based meshing approach. This equates to detecting the iso-surface of a segmented 3D image in the context of image-based pore-scale modelling. The job of extracting an iso-surface from a regular grid is a significant challenge with numerous applications in visualisation, graphics, and vision [73]. CAD based meshing approach is also attributed to poor triangle quality, likelihood to overestimate surface area and to over triangulate based on a sample density equal to voxel size [74].

Instead of conformally meshing complex shapes, the novel diffuse interface approach can be used. It's a type of immersed boundary method in which the complicated geometry is surrounded in a structured non-conforming mesh and a phase field is mapped to the mesh's nodes as shown in Figure 8. The phase field ϕ is a scalar field that varies smoothly from zero to one at the complex geometry's border and is equal to one on mesh elements inside the simulation domain and zero on mesh elements outside the concerned geometry. For porous domain, that would be one in the pore space and zero inside solid matrix. The region where magnitude of gradient of the phase field, $|\nabla\phi| > 0$ is the diffuse boundary region and the original sharp boundary of geometry is found at scalar value of phase field $\phi = 0.5$.

Using a finite element method with weakly defined governing equations like volume and surface integrals, diffuse interface boundary value problems on exceedingly complex domains can be solved without explicitly parameterizing boundary and interface surfaces. From Nguyen et al's work [10], following identities are used to convert volume integrals on Ω and surface integrals on $\partial\Omega$ to volume integrals on κ:

$$\int_\Omega A d\Omega = \int_\kappa A H d\Omega \approx \int_\kappa A \phi d\Omega \qquad (2.37)$$

26

$$\int_{\partial\Omega} B d\partial\Omega = \int_{\kappa} \delta_{\partial\Omega} B d\Omega \approx \int_{\kappa} B|\nabla\phi| d\Omega \qquad (2.38)$$

$$\boldsymbol{n} \approx -\frac{\nabla\phi}{|\nabla\phi|} \qquad (2.39)$$

where Ω is the complex geometry with boundary $\partial\Omega$, κ is the structured surrounding domain, H is a Heaviside function, $\delta_{\partial\Omega}$ is a Dirac delta function and n is the outward facing normal. H and $\delta_{\partial\Omega}$ are approximated by ϕ and $|\nabla\phi|$ respectively.
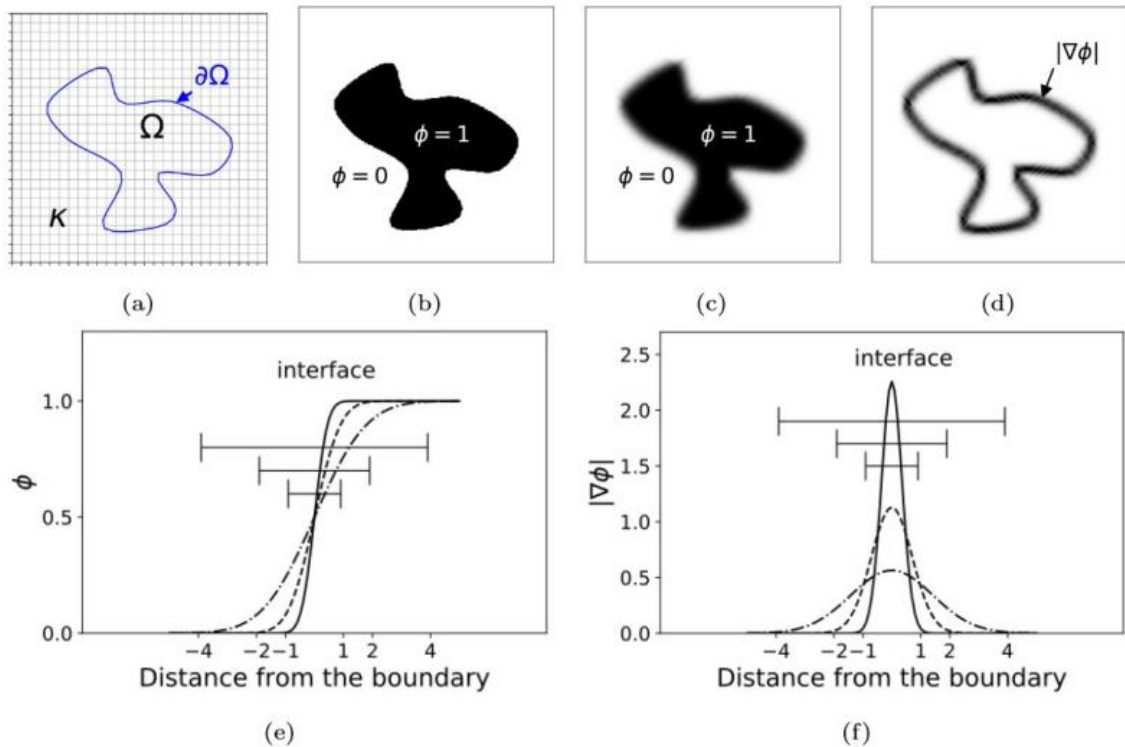
Figure 8: Domain Ω surrounded with larger structured mesh κ in (a), binary phase field representation of geometry in (b), phase field with a diffuse interface in (c), gradient of diffuse interface approximated by $|\nabla\phi|$ in (d), different phase fields ϕ and $|\nabla\phi|$ variation with distance from boundary in (e) and (f). This figure was taken from Monte et al [11].

The ability to employ structured quadrilateral/hexahedral meshes for any complicated geometry is the fundamental benefit of an immersed boundary approach such as diffuse interface method, as opposed to unstructured meshes generated from CAD files, which have stability difficulties and require a lot of time and effort. The absence of mesh conformance to the complex geometry boundary, on the other hand, has a detrimental impact on simulation accuracy. Boundary conditions are spread across numerous mesh components, curving boundaries take on a step-like appearance, and the apparent scale of complex geometry changes. Previous work by Nguyen et al. has addressed this issue by altering the integration schemes within mesh elements including the complex geometry boundary, as with cut cell approaches [14], or by greatly refining the mesh near the complex geometry boundary [10]. Though, adaptive mesh refining technique adds up to the computational complexity and time of the simulation process. Additionally, porous media geometries have high surface area and irregulars features at interface which makes adaptive mesh refining unsuitable for diffuse interface method. This work focuses on using diffuse interface method on complex pore structures of porous media using OpenCMP's implementation [16] without adaptive mesh refining at interfaces and reaching acceptable accuracy by optimising the various parameters as explained in Methodology section of the work. Section 2.4.1 and 2.4.2 present derivation of weak forms for Poisson and incompressible Navier Stokes equation for diffuse interface method respectively as needed for the project.

2.4.1 Poisson Equation

Starting with the Poisson equation:

$$-\nabla^2 u = f \ \text{ in } \ \Omega \tag{2.40}$$

where u is an unknown function, f is a forcing function and Ω is the domain. Considering the following boundary conditions:

$$u = g \ \text{ on } \partial\Omega_D \tag{2.41}$$

$$-\boldsymbol{n}.\boldsymbol{\nabla}\,u = h \ \ on \ \partial\Omega_N \qquad\qquad (2.42)$$

$$-\boldsymbol{n}.\boldsymbol{\nabla}\,u = r(u-q) \ \ on \ \partial\Omega_R \qquad\qquad (2.43)$$

where $\partial\Omega_D, \partial\Omega_N$ and $\partial\Omega_R$ are Dirichlet, Neumann and Robin conditions respectively.

Continuing from the weak form derived in section 2.3.1, the equation (2.24):

$$\int_{\Omega}(\boldsymbol{\nabla}u).(\boldsymbol{\nabla}v) - \int_{\partial\Omega_N} vh - \int_{\partial\Omega_R} vr(u-q) = \int_{\Omega} fv \qquad\qquad (2.44)$$

Now to move from conformal domain Ω to structured grid domain κ, a phase field ϕ is defined with value of one on the mesh elements inside Ω and zero outside Ω. There is a smooth transition of ϕ from zero to one across the boundary $\partial\Omega$. From Nguyen et al's work [10], following identities are used to convert volume integrals on Ω and surface integrals on $\partial\Omega$ to volume integrals on κ:

$$\int_{\Omega} Ad\Omega = \int_{\kappa} AHd\Omega \approx \int_{\kappa} A\phi d\Omega \qquad\qquad (2.45)$$

$$\int_{\partial\Omega} Bd\partial\Omega = \int_{\kappa} \delta_{\partial\Omega} Bd\Omega \approx \int_{\kappa} B|\boldsymbol{\nabla}\phi|d\Omega \qquad\qquad (2.46)$$

$$\boldsymbol{n} \approx -\frac{\boldsymbol{\nabla}\phi}{|\boldsymbol{\nabla}\phi|} \qquad\qquad (2.47)$$

where H is a Heaviside function, $\delta_{\partial\Omega}$ is a Dirac delta function and n is the outward facing normal. They are approximated by ϕ and $|\boldsymbol{\nabla}\phi|$ respectively.

Substituting these identities into (2.44):

$$\int_\kappa \nabla u \cdot \nabla v\phi + \int_\kappa vh|\nabla\phi|\phi_N - \int_\kappa vr(u-q)|\nabla\phi|\,\phi_R = \int_\kappa fv\phi \qquad \textbf{(2.48)}$$

where ϕ_N and ϕ_R correspond to portions of phase field with Neumann and Robin boundary conditions respectively [11].

Since, the κ mesh does not conform to the edge of interface, Dirichlet boundaries can not be applied by setting value of trial function v at the interface. To apply the Dirichlet boundary conditions, the Nitsche Method [10] is used to weakly impose in the $\partial\Omega_D$ region of the interface. The Poisson equation weak form after adding Nitsche terms becomes:

$$\int_\kappa \nabla u \cdot \nabla v\phi + \int_\kappa vh|\nabla\phi|\phi_N - \int_\kappa vr(u-q)|\nabla\phi|\,\phi_R - \int_\kappa vf\phi \ +$$
$$\int_\kappa (u-g)\nabla\phi \cdot \nabla v\phi_D + \int_\kappa v\nabla\phi \cdot \nabla u\phi_D + \beta \int_\kappa v(u-g)|\nabla\phi|\phi_D = 0 \qquad \textbf{(2.49)}$$

where β is the penalty parameter, $\beta = \frac{10n^2}{h}$, n is the polynomial interpolant order and h is the mesh element size.

2.4.2 Incompressible Navier Stokes Equation

Starting with momentum equation on a domain Ω:

$$\frac{\partial \boldsymbol{u}}{\partial t} - \nu\nabla^2\boldsymbol{u} + (\boldsymbol{u} \cdot \nabla)\boldsymbol{u} + \nabla p = \boldsymbol{f} \ \text{in } \Omega \qquad \textbf{(2.50)}$$

where ν is kinematic viscosity and $\boldsymbol{f}$ is some body force.

The following boundary conditions are considered:

$$\boldsymbol{u} = \boldsymbol{g} \ \text{ on } \partial\Omega_D \qquad \textbf{(2.51)}$$

$$-\boldsymbol{n}.(\nu\nabla\boldsymbol{u} - p) = \boldsymbol{h} \ \text{ on } \partial\Omega_N \qquad \textbf{(2.52)}$$

$$-\boldsymbol{n}.(\nu\nabla\boldsymbol{u} - \ p) = \boldsymbol{r}(\boldsymbol{u} - q) \ \text{ on } \partial\Omega_R \qquad \textbf{(2.53)}$$

Continuing from the weak form derived in section 2.3.2, the equation (2.35) and equation (2.36):

$$\int_\Omega \frac{\partial \boldsymbol{u}}{\partial t} \cdot \boldsymbol{v} + \int_\Omega \nu \boldsymbol{\nabla} \boldsymbol{u} \cdot \boldsymbol{\nabla} \boldsymbol{v} + \int_\Omega (\boldsymbol{u} \cdot \boldsymbol{\nabla})\boldsymbol{u} \cdot \boldsymbol{v} - \int_\Omega p \boldsymbol{\nabla} \cdot \boldsymbol{v} - \int_\Omega q \boldsymbol{\nabla} \cdot \boldsymbol{u} =$$

(2.54)

$$\int_\Omega \boldsymbol{f} \cdot \boldsymbol{v} + \int_{\partial\Omega_N} \boldsymbol{h} \cdot \boldsymbol{v} + \int_{\partial\Omega_R} r(\boldsymbol{u} - q) \cdot \boldsymbol{v} \quad \text{for} \quad \boldsymbol{v} \in V \text{ and } q \in Q$$

Now to move from conformal domain Ω to structured grid domain κ, a phase field ϕ is defined with value of one on the mesh elements inside Ω and zero outside Ω. There is a smooth transition of ϕ from zero to one across the boundary $\partial\Omega$. From Nguyen et al's work, following identities are used to convert volume integrals on Ω and surface integrals on $\partial\Omega$ to volume integrals on κ:

$$\int_\Omega A d\Omega = \int_\kappa AH d\Omega \approx \int_\kappa A\phi d\Omega \tag{2.55}$$

$$\int_{\partial\Omega} B d\partial\Omega = \int_\kappa \delta_{\partial\Omega} B d\Omega \approx \int_\kappa B|\boldsymbol{\nabla}\phi| d\Omega \tag{2.56}$$

$$\boldsymbol{n} \approx -\frac{\boldsymbol{\nabla}\phi}{|\boldsymbol{\nabla}\phi|} \tag{2.57}$$

where H is a Heaviside function, $\delta_{\partial\Omega}$ is a Dirac delta function and n is the outward facing normal. They are approximated by ϕ and $|\boldsymbol{\nabla}\phi|$ respectively. Substituting these identities into (2.54):

$$\int_\kappa \frac{\partial \boldsymbol{u}}{\partial t} \cdot \boldsymbol{v}\phi + \int_\kappa \nu \boldsymbol{\nabla} \boldsymbol{u} \cdot \boldsymbol{\nabla} \boldsymbol{v}\phi + \int_\kappa (\boldsymbol{u} \cdot \boldsymbol{\nabla})\boldsymbol{u} \cdot \boldsymbol{v}\phi - \int_\kappa p \boldsymbol{\nabla} \cdot \boldsymbol{v}\phi - \int_\kappa q \boldsymbol{\nabla} \cdot \boldsymbol{u}\phi \tag{2.58}$$

$$= \int_\kappa \boldsymbol{f} \cdot \boldsymbol{v}\phi + \int_\kappa \boldsymbol{h} \cdot \boldsymbol{v}|\boldsymbol{\nabla}\phi|\phi_N + \int_\kappa \boldsymbol{r}(\boldsymbol{u} - q) \cdot \boldsymbol{v}|\boldsymbol{\nabla}\phi|\phi_R$$

where ϕ_N and ϕ_R correspond to portions of phase field with Neumann and Robin boundary conditions respectively [11].

Since, the κ mesh does not conform to the edge of interface, Dirichlet boundaries can not be applied by setting value of trial function v at the interface. To apply the Dirichlet boundary conditions, the Nitsche Method is used to weakly impose in the $\partial\Omega_D$ region of the interface. The Incompressible Navier Stokes equation weak form after adding Nitsche terms becomes:

$$\int_\kappa \frac{\partial \boldsymbol{u}}{\partial t} \cdot \boldsymbol{v}\phi + \int_\kappa \nu\boldsymbol{\nabla}\boldsymbol{u} \cdot \boldsymbol{\nabla}\boldsymbol{v}\phi + \int_\kappa (\boldsymbol{u} \cdot \boldsymbol{\nabla})\boldsymbol{u} \cdot \boldsymbol{v}\phi - \int_\kappa p\boldsymbol{\nabla} \cdot \boldsymbol{v}\phi - \int_\kappa q\boldsymbol{\nabla} \cdot \boldsymbol{u}\phi$$

$$= \int_\kappa \boldsymbol{f} \cdot \boldsymbol{v}\phi + \int_\kappa \boldsymbol{h} \cdot \boldsymbol{v}|\boldsymbol{\nabla}\phi|\phi_N + \int_\kappa \boldsymbol{r}(\boldsymbol{u} - q) \cdot \boldsymbol{v}|\boldsymbol{\nabla}\phi|\phi_R \qquad \textbf{(2.59)}$$

$$+ \int_\kappa (\boldsymbol{u} - \boldsymbol{g})\boldsymbol{\nabla}\phi \cdot \boldsymbol{\nabla}\boldsymbol{v}\phi_D + \int_\kappa \nu\boldsymbol{\nabla}\phi \cdot \boldsymbol{\nabla}\mathbf{u}\phi_D + \beta \int_\kappa \boldsymbol{v}(\boldsymbol{u} - \boldsymbol{g})|\boldsymbol{\nabla}\phi|\phi_D$$

where β is the penalty parameter, $\beta = \frac{10n^2}{h}$, n is the polynomial interpolant order and h is the mesh element size.

3 METHODOLOGY

This chapter starts with the procedure to artificially generate two dimensional binary images of porous media. This is followed by the two meshing methods – conformal and phase field on structured quadrilateral mesh and their description. The meshing methods are followed by formulation of the partial differential equations used to model mass diffusion and incompressible steady state fluid flow. Then, the initial and boundary conditions are formulated to best simulate the physical experiments, consistent solver settings are used throughout the simulations. Finally, reference solutions are simulated for all the images of different porosities on a conformal mesh for comparison to simulation results from diffuse interface method in Chapter 4.

3.1 Image generation

Since the work in the present thesis represents a first proof-of-concept, the images used were simple sphere packings artificially generated as follows. Following similar methodology, two additional images with different porosities are generated to demonstrate the numerical models and determine properties. The image is two dimensional, generated via open-source python package Porespy [75]. To generate the image, solid spheres are inserted in an empty NumPy array of size 1000×1000. The image resolution is hence 1000×1000. Six solid spheres of radius 100 pixels and two solid spheres of radius 150 pixels are inserted. Each pixel in the pore space is assigned the binary value of '1' and each pixel in solid space is assigned a value of '0'. The image is a square lattice of spacing $1\ \mu m$ in each pixel. Hence, $1000\ \mu m$ or $1mm$ in each direction which matches the dimensions of typical tomography images of porous media. Porosity of the image is determined by taking a sum of NumPy array divided by the size of array 10^6.

$$\varepsilon = \frac{sum\ of\ array}{array\ size} \qquad \text{(3.1)}$$

The porosity of Figure 9 is determined to be 0.6703. Two additional images with porosity 0.60 and 0.49 are generated similarly as shown in Figure 10.
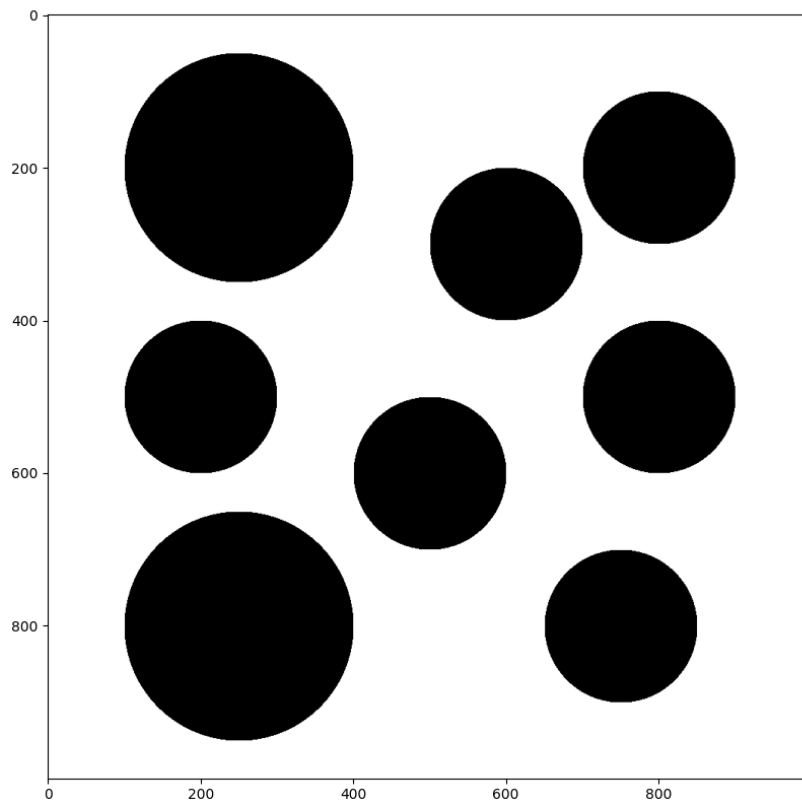
Figure 9: A 2D binary image representing porous medium
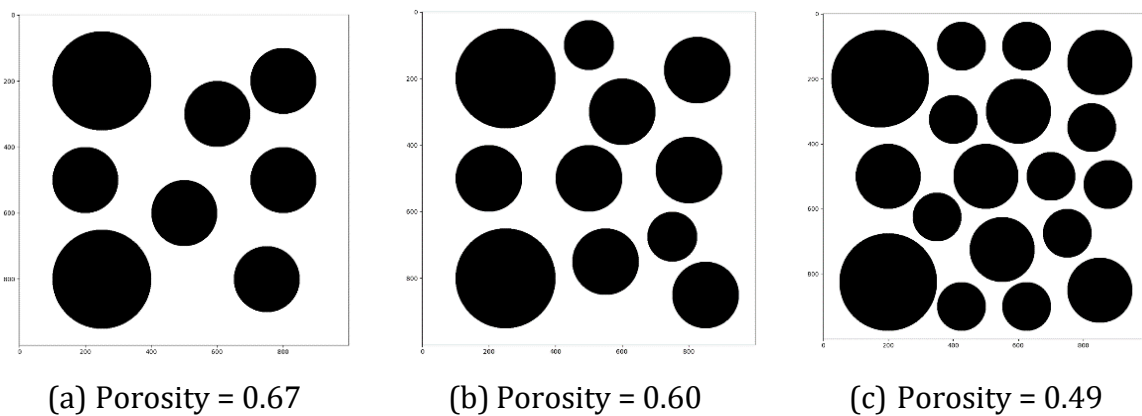
| (a) Porosity = 0.67 | (b) Porosity = 0.60 | (c) Porosity = 0.49 |

Figure 10: Three different porous media images with varying porosities

3.2 Meshing

This section discusses the two meshing methods used to determine transport properties- tortuosity, permeability, and inertial constant. An unstructured conformal mesh is generated with all the models applied to act as reference solutions to diffuse interface method solutions followed by generation of structured quadrilateral mesh with mapped phase field.

3.2.1 Conformal Triangular Mesh

As discussed in the background section of the thesis work, an unstructured conformal mesh is traditionally used with porous media geometries for solving with numerical scheme like finite element method. Unstructured conformal meshes with varying mesh densities – coarse to fine are generated using $GMSH$ [54] – a meshing software as shown in Figure 11. $GMSH$ generates a triangular mesh compatible with $NGSolve$ [76] and $OpenCMP$ [16]. GMSH is also used to label the physical boundaries, namely- 'inlet', 'outlet' and 'walls' as shown in Figure 12 which define the inlet boundary, outlet boundary and the solid matrix, isolated parallel boundaries of the pore structure respectively.
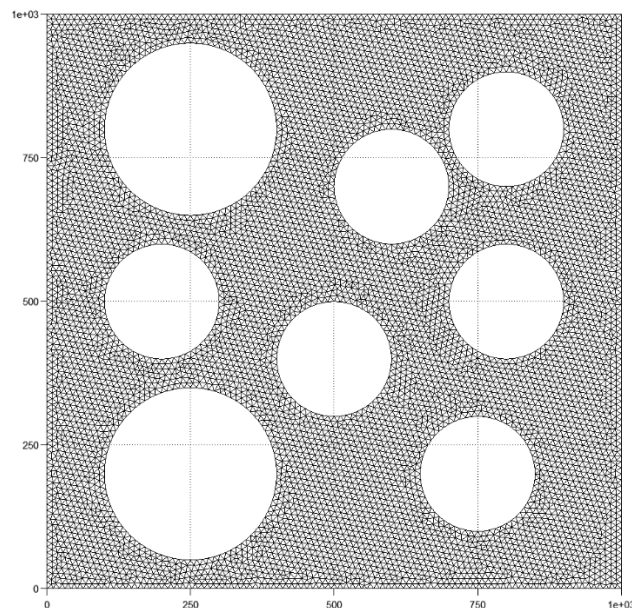
Figure 11: 2D conformal mesh representing porous medium generated using $GMSH$

35
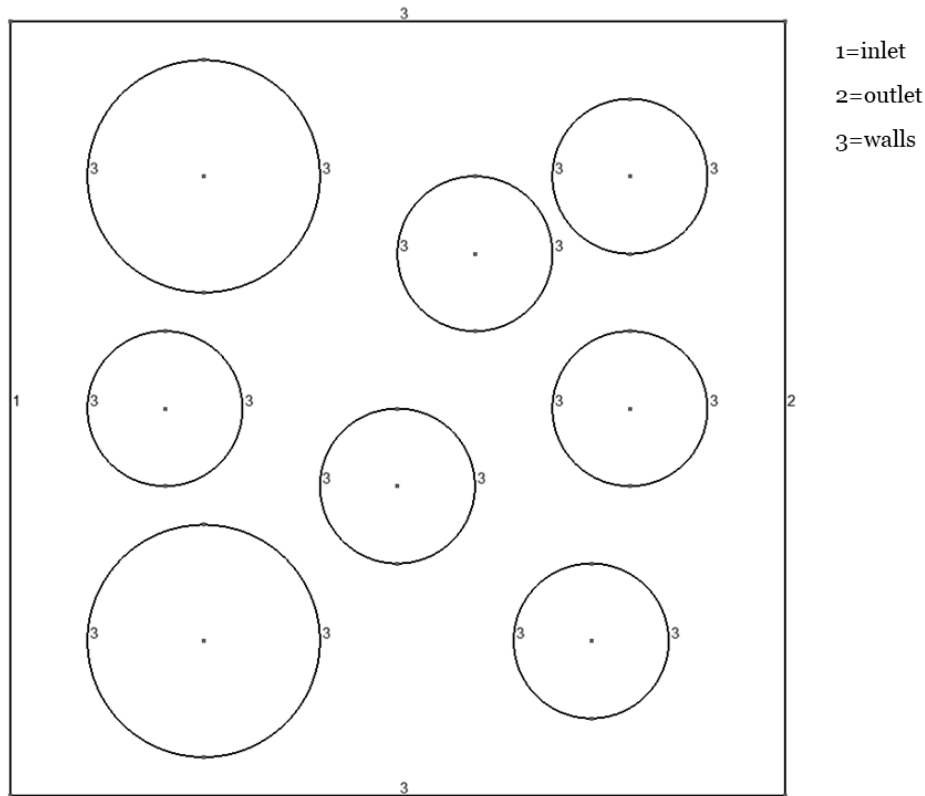
Figure 12: Boundary labels applied on the conformal mesh using *GMSH*

3.2.2 Phase field mapped on a Structured Quadrilateral Mesh

Phase field (ϕ) is a scalar field equal to zero on the mesh elements inside the solid domain and one in the pore space with smooth transition from zero to one at interface depending upon the chosen width of diffuse interface. Starting with original 2-dimensional binary NumPy image as shown in Figure 9, the border of the solid objects is extracted by subtracting original image from an image eroded by a single pixel. Then, a Euclidean distance transform of the solid border is taken using python package *edt* [77] Finally, an error function is used on the distance transform of the border from python package SciPy [78] to generate smooth transition of phase field from zero inside the solids to one in void space at the interface. The width of diffuse interface is controlled by a parameter – lambda. The phase field is then projected on a structured quadrilateral mesh for *NGSolve*.

The different parameters affecting the phase field mapped on quadrilateral mesh are discussed in detail in section 3.3.
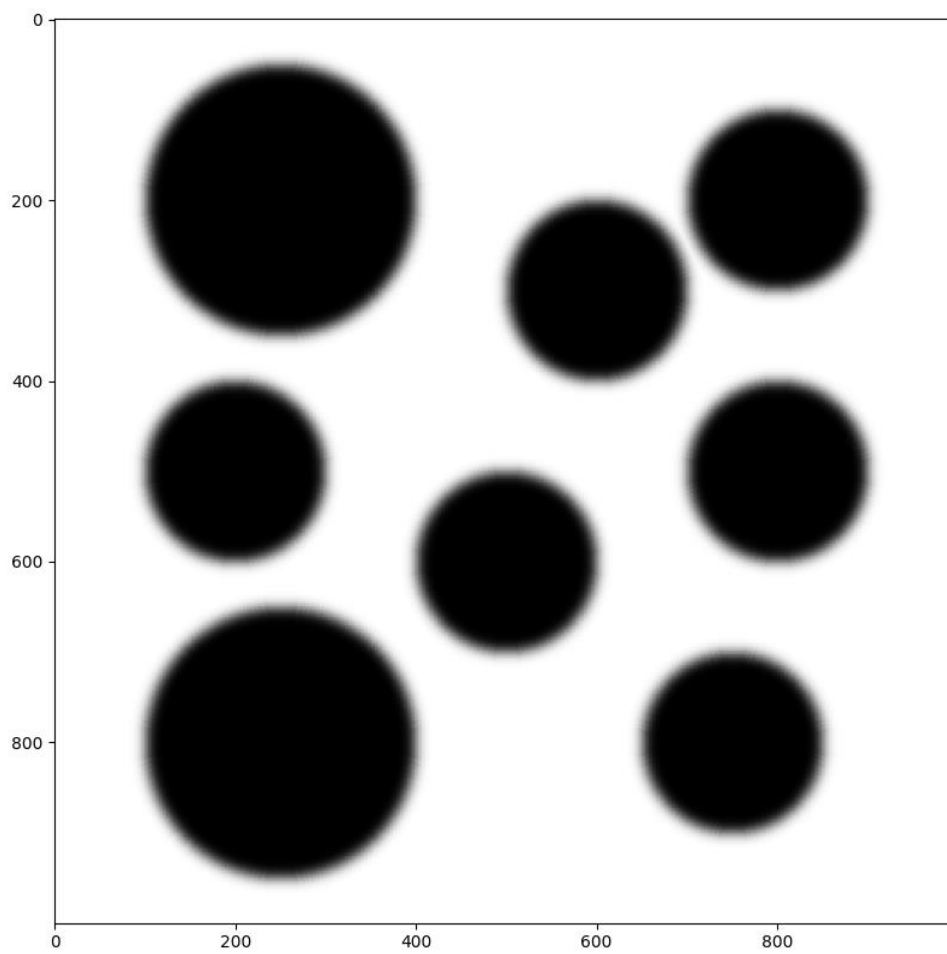
Figure 13: 2D NumPy array representing phase field

3.3 Diffuse Interface Method Parameters

The following parameters are defined to construct the structured quadrilateral mesh and phase field grid function with NumPy array interpolated onto it. The phase fields are demonstrated by an example image of a circle with binary value of one outside circle domain and zero inside.

3.3.1 Lambda (λ)

To generate a smooth transition of phase field from zero inside solids to one outside, an error function from the SciPy python package [78] is used:

$$\operatorname{erf}(z) = \frac{2}{\sqrt{\pi}} \int e^{-t^2} , t = 0..z \tag{3.2}$$

where z in erf(z) is the NumPy array of ratio of distance transform and lambda (λ). Lambda (λ) is used to vary the extent of phase field transition smoothening at the interface. Two times lambda (λ) corresponds to the number of pixels taken by width of diffuse interface in the original image resolution i.e., 1000 x 1000.

3.3.2 Coarseness Ratio

Coarseness Ratio is defined as the ratio between image resolution and the structured quadrilateral mesh scale.

$$Coarseness\ Ratio = \frac{Image\ Resolution}{Structured\ Mesh\ Scale} \tag{3.3}$$

Coarseness ratio can be related to the coarseness of the structured mesh. Higher ratio indicates coarser mesh and vice versa. The image resolution is chosen to be 1000 x 1000 and mesh scale is varied. A high image resolution gives the best approximation of curved boundaries. Coarseness ratio directly affects the number of elements in the mesh, the accuracy of the simulation compared to conformal mesh solutions and most importantly

the stability of the simulation. For example, Figure 14 shows a structured mesh with coarseness ratio of ten i.e., mesh scale of 100×100.
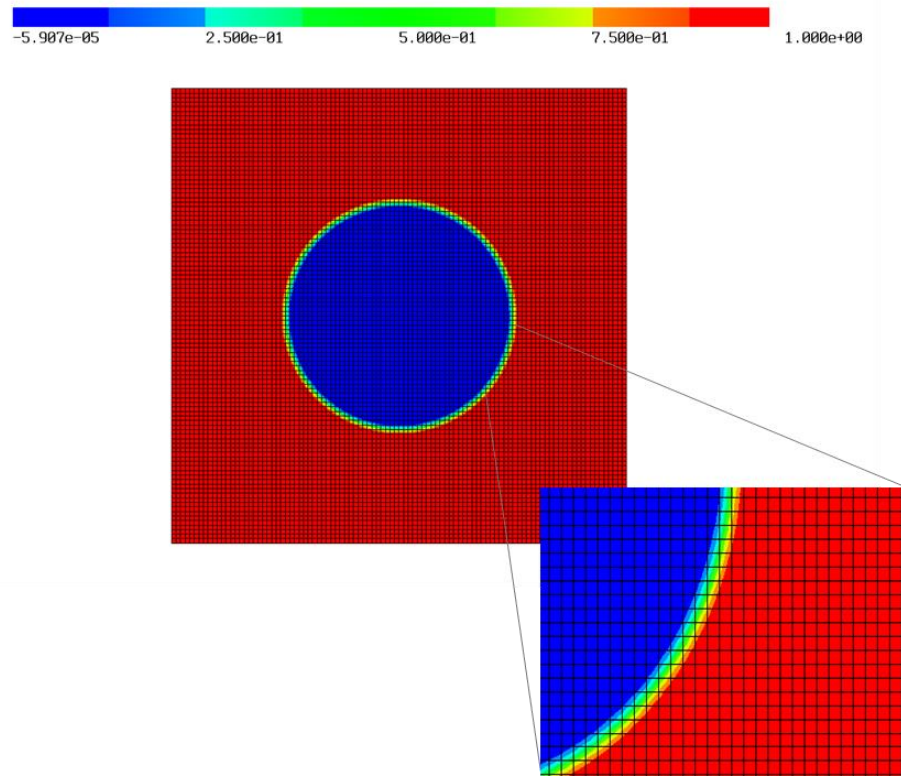
Figure 14: Diffuse Interface Phase Field with $coarseness\ ratio\ =\ 10$

3.3.3   Diffuse Interface Width

The number of structured mesh elements of the phase field (ϕ) grid function where the value of phase field is varying between zero inside the solids to one in the void/pore space is termed as diffuse interface width. Magnitude of gradient of phase field, $|\nabla\phi|$ is greater than zero in the region of diffuse interface boundary. Diffuse interface width of the structured mesh can be calculated as:

$$Diffuse\ Interface\ Width = \frac{2\lambda}{Coarseness\ Ratio} \tag{3.4}$$

39

Figure 15 demonstrates gradient of phase field on structured mesh with coarseness ratio of ten i.e., mesh scale of 100×100 with varying diffuse interface width from four to half mesh elements. Large values of DI width extend the boundary condition constraints into the interior of the complex geometry or into the void space depending on the type of boundary condition- Neumann or Dirichlet respectively. DI width smaller than one mesh elements does not present a smooth gradient of phase field ϕ at the boundaries leading to numerical approximation errors.
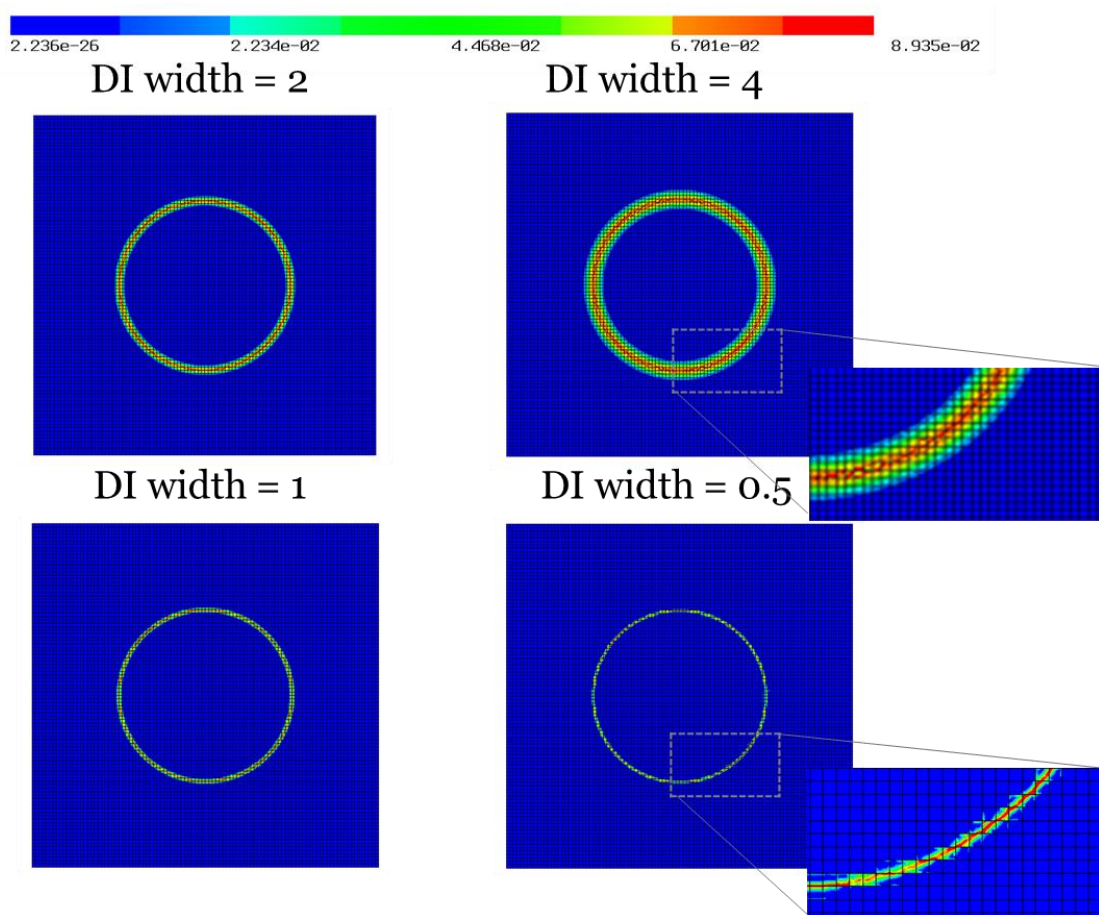
Figure 15: Gradient of phase field on structured mesh with varying DI width

3.4 Model Formulation

3.4.1 Tortuosity

Diffusional tortuosity is determined by comparing the steady-state diffusive fluxes passing through the porous media space and the free homogeneous space with the same dimensions. A constant concentration difference is applied between *inlet* and *outlet* boundary faces, while the other two faces parallel to the diffusional flow direction are set as solid walls for purpose of isolation.

Driven by the constant concentration gradient, the diffusive specie moves from the inlet face to the outlet face. At steady state, the diffusional mass flux passing through the porous media space and the free homogeneous space can be obtained from Fick's law:

Fick's first law for flux in single direction can be stated as:

$$J_d^{(Pore)} = -AD_{eff}\nabla C \tag{3.5}$$

$$J_d^{(Free)} = -AD_{bulk}\nabla C \tag{3.6}$$

where $J_d^{(Pore)}$ and $J_d^{(Free)}$ are the diffusion fluxes passing through the porous media space and free homogenous space respectively.

Fick's second law:

$$\frac{\partial C}{\partial t} = \nabla \cdot (D_{bulk}\nabla C) \tag{3.7}$$

The Dirichlet boundary conditions are:

$C = 1\ mol/m^3$ at *inlet*

$C = 0\ mol/m^3$ at *outlet*

Now, the steady state Fick's first Law can be compared to a steady state Poisson equation with source term $f = 0$.

$$\nabla^2 C = 0 \tag{3.8}$$

Neumann no flux boundary condition at pore-solid interface *walls* is set as:

$$\nabla C \cdot \mathrm{n} = 0 \tag{3.9}$$

From equation (2.10), taking the ratio of $J_d^{(Pore)}$ and $J_d^{(Free)}$, Tortuosity τ can be expressed as:

$$\tau = \frac{J_d^{(Free)}}{J_d^{(Pore)}} \varepsilon = \frac{D_{bulk}}{D_{eff}} \varepsilon \tag{3.10}$$

Table 2 summarises the list of parameters with numerical values where applicable and consistent units.

Table 2: List of parameters used in determination of tortuosity with constant values and units

Parameter	Variable	Value	Units
Length	L	1000	μm
Concentration	C	—	mol/m^3
Bulk Diffusivity	D_{bulk}	1	mm^2/s
Effective Diffusivity	D_{eff}	—	mm^2/s
Concentration flux	J_d	—	$(mol/m^2 s)$
Porosity	ε	—	—

3.4.2 Permeability and Inertial Constant

Permeability and initial constant of a porous medium image is determined by conducting many incompressible fluid flow simulations at varying inlet velocities and measuring the pressure drop for each specific inlet velocity between *inlet* and *outlet* boundary faces. The quadratic relationship between pressure gradient and inlet velocities as shown in equation (3.11) is plotted and coefficients determined from the plot are used to determine permeability and inertial constant. The coefficient of the linear velocity term called Darcy coefficient is used to determine permeability as shown in equation (3.12) and the coefficient of quadratic velocity term called Forchheimer coefficient is used to determine inertial constant as shown in equation (3.13).

Darcy-Forchheimer relationship:

$$-\nabla p = \boldsymbol{a} \cdot \mathbf{v} + \boldsymbol{b} \cdot \mathbf{v}^2 \qquad (3.11)$$

where $\boldsymbol{a}$ represents Darcy coefficient and $\boldsymbol{b}$ represents Forchheimer coefficient. Darcy and Forchheimer coefficients are vector quantities for any porous media since they depend on the direction of fluid flow. They can be defined for a single direction as:

$$a = \frac{\mu}{K} \qquad (3.12)$$

$$b = \beta\rho \qquad (3.13)$$

where μ is fluid dynamic viscosity, K is the porous media permeability, ρ is fluid density and β is inertial constant. It is also established that coefficient a represents the intrinsic permeability of the porous media because of inverse relationship to permeability [46]–[48] whereas, coefficient b depends on the geometrical properties of porous media and needs to be determined by experiments or simulations.

The steady state incompressible Navier—Stokes equations is modelled as follows:

$$\boldsymbol{\nabla}.\,\mathbf{v} = 0 \qquad\qquad (3.14)$$

$$\boldsymbol{\nabla}.\,(\mathbf{vv}) - \nu\nabla^2\mathbf{v} + \boldsymbol{\nabla}p = 0 \qquad\qquad (3.15)$$

where $\mathbf{v}$ represents velocity vector, ν represents kinematic viscosity and p represents scalar pressure field.

The Dirichlet boundary conditions are:

$v = 0.05 - 0.15\ m/s$ at $inlet$

Inlet velocities are selected from the Forchheimer regime.

$v = 0\ m/s$ at $walls$ that is no slip condition on solid interface

No stress outlet boundary condition is set at the $outlet$:

$$\boldsymbol{n} \cdot (\mathbf{vv} - \nu\boldsymbol{\nabla}\mathbf{v} + pI) - \max(\mathbf{v}\cdot\boldsymbol{n}, 0)\,\mathbf{v} = \mathbf{0} \qquad\qquad (3.16)$$

To handle the non-linear convection term in equation (3.15), Oseen style linearization is done:

$$\boldsymbol{\nabla}\cdot(\mathbf{vv}) \rightarrow \boldsymbol{\nabla}\cdot(\mathbf{v}\boldsymbol{w}) \qquad\qquad (3.17)$$

where $\boldsymbol{w}$ is a known velocity field which is taken as the solution of the previous iteration. The relative non-linear tolerance for Oseen linearization is set as 1×10^{-4} or after four iterations.

Table 3 summarises the list of parameters with numerical values where applicable and consistent units.

Table 3: List of parameters used in determination of permeability and inertial constant with constant values and units

Parameter	Variable	Value	Units
Length	L	1000	μm
Velocity	v	0.05 – 0.15	m/s
Kinematic viscosity	ν	1	mm^2/s
Dynamic viscosity	μ	10^{-3}	$Pa\ s$
Density	ρ	1000	Kg/m^3
Pressure	p	—	Pa
Permeability	K	—	m^2
Inertial constant	β	—	m^{-1}

3.5 Using Finite Element Method on conformal mesh

This section will discuss results on a conformal mesh based on simulations conditions described in section 3.4. Models as are implemented on three geometries with varying porosities as shown in Figure 10 to determine the properties from mass diffusion and incompressible Navier Stokes fluid flow.

Conformal meshes are generated with similar mesh density for the three images using *GMSH* as presented in Figure 16:
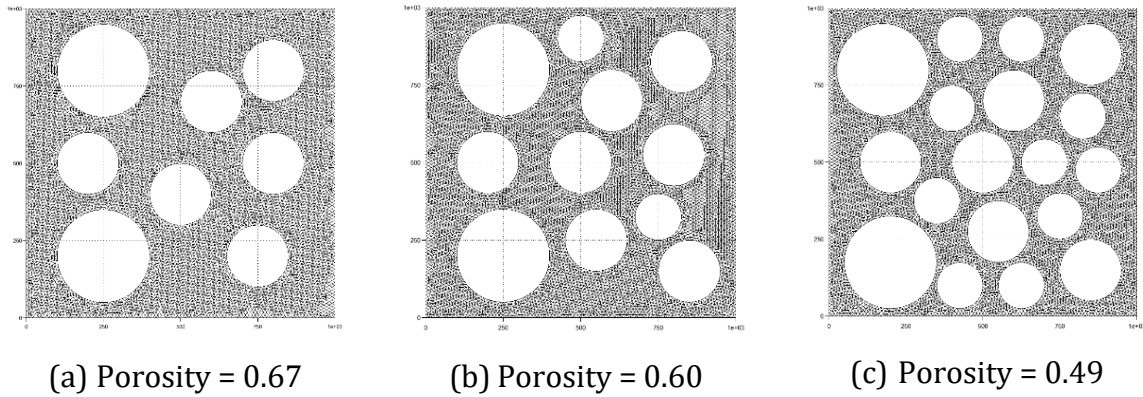

(a) Porosity = 0.67   (b) Porosity = 0.60   (c) Porosity = 0.49

Figure 16: Conformal meshes of three different porous media geometries with varying porosity and same mesh density

3.5.1 Tortuosity of Porous Media

For conducting the finite element simulation for Poisson equation (3.8) with Dirichlet boundaries at *inlet* and *outlet* and Neumann boundaries at *walls*, OpenCMP was used. Starting with types of finite element spaces, Poisson simulation uses standard H1 finite element space for scalar variable with polynomial order equal to three. Choice of solver and preconditioner are set as *direct*. The output simulation result file is saved in .vtu format for visualization in *Paraview* – an open-source, multi-platform data analysis and visualization application [79]. Number of subdivisions in the .vtu file is set to be equal to polynomial order of the H1 space that is, three. Simulation settings are summarised in Table 4.

Table 4: Simulation settings for Poisson equation to determine Tortuosity

Finite element space	H1
interpolant order	3
solver	direct
preconditioner	direct
.vtu subdivisions	3

Mass flux is measured at *inlet* and *outlet* boundaries from the simulations using *Paraview*. The mass flux determined from simulations is then substituted into equation (3.10) to determine tortuosity. The simulation settings are kept same for simulation on a conformal mesh and a structured quadrilateral mesh with phase field for diffuse interface method. Results from a conformal mesh are presented as follows for reference comparison to diffuse interface method results in chapter 4. Figure 17 and Figure 18 show the *Paraview* visualization of concentration fields with above mentioned conditions for the geometries with different porosities. Concentration field can be seen varying from 1 to 0 from *inlet* to *outlet* across the domain.

46

Figure 17: Concentration field visual from simulation on conformal mesh
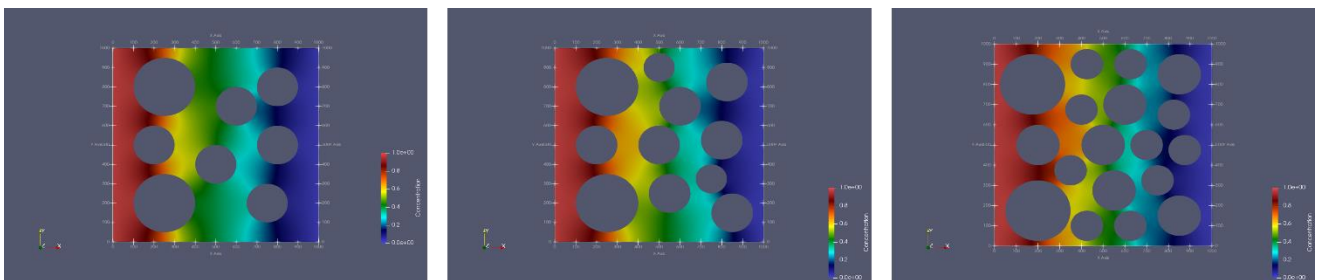
Figure 18: Concentration field for images with varying porosities on conformal mesh

Figure 19 and Figure 20 show the *Paraview* visualization of magnitude of concentration gradient fields with above mentioned conditions for the geometries with different porosities. Concentration gradient field can be seen varying from 1×10^{-3} to 0 across the domain. Concentration gradient is determined to measure the total concentration flux by integrating the gradient across boundaries. It is observed that the concentration flux is same at *inlet* and *outlet* boundaries which is true for conservation of mass across simulation domain.

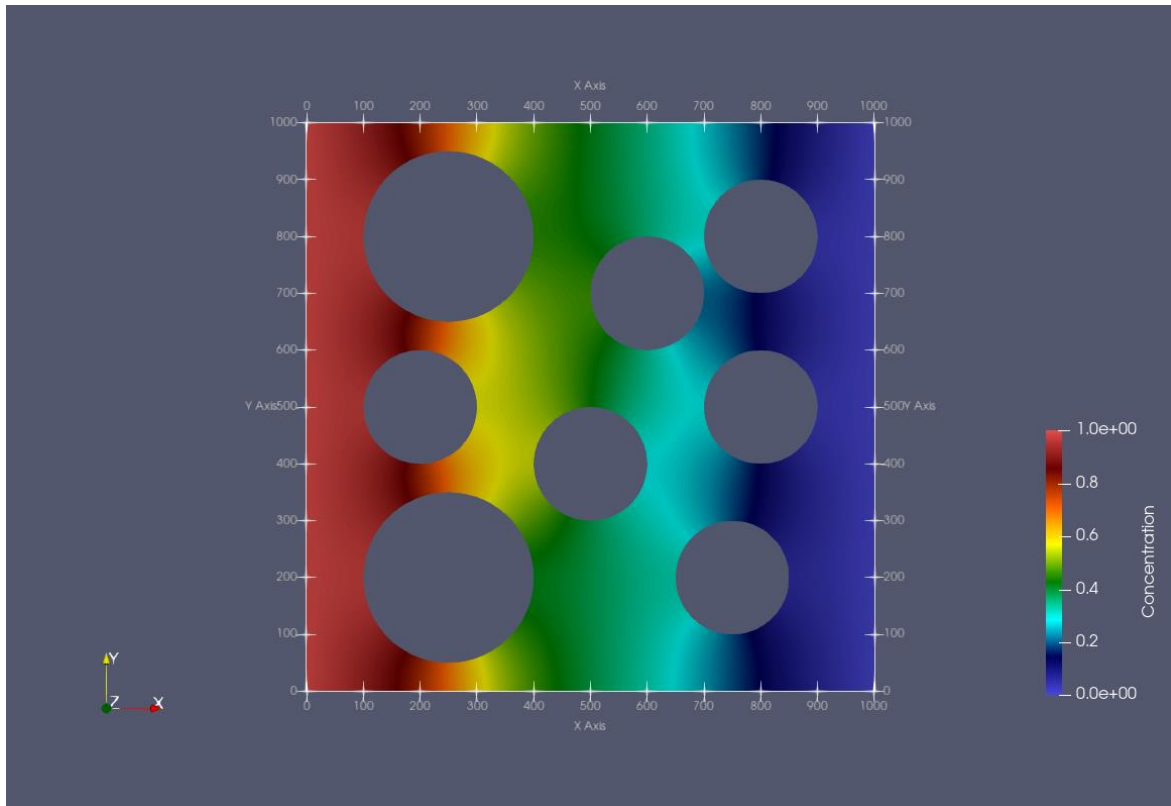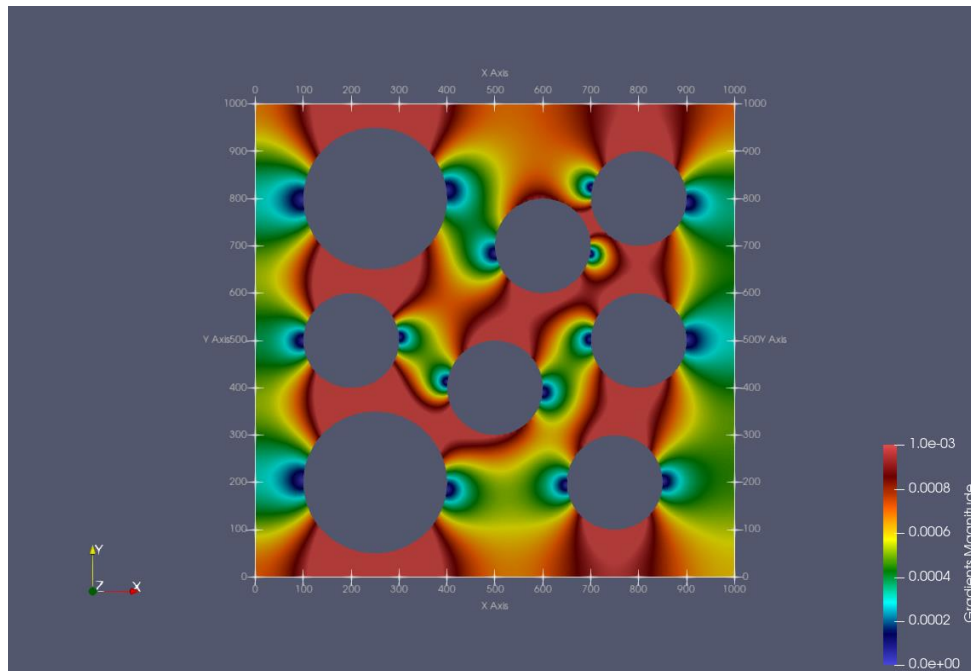**Figure 19: Concentration gradient field visual from simulation on conformal mesh**
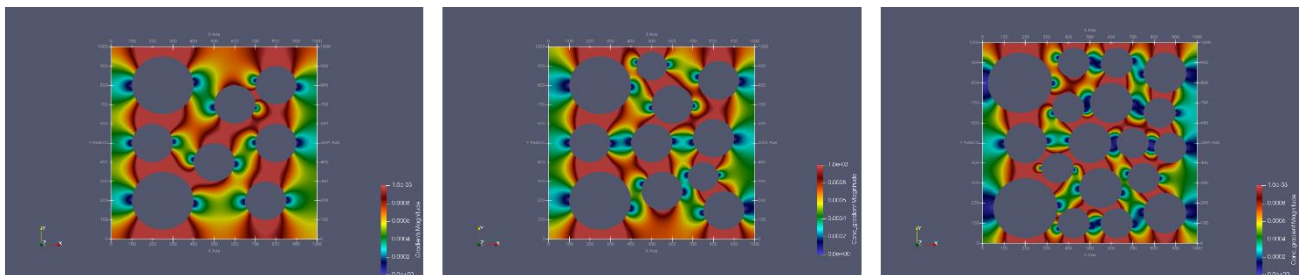
Figure 20: Concentration gradient field visual for images with varying porosities on conformal mesh

The solution was also made to be mesh independent by determining tortuosity on conformal meshes at varying mesh density- from coarse to fine. The relative error is defined as-

$$relative\ error = \frac{\tau - \tau_{ref}}{\tau_{ref}} \qquad (3.18)$$

where, τ is the tortuosity at present mesh and τ_{ref} is the tortuosity at finest mesh.

Relative error in tortuosity is allowed to reach tolerance of 1×10^{-3} as shown in Table 5 and Figure 21. The mesh density at this tolerance is used for conformal meshes for porous media geometries with porosities equal to 0.60 and 0.49 as well.

Table 5: Reaching mesh independence for mass diffusion on conformal mesh with porosity = 0.67

Number of elements	Conc. flux at inlet	Conc. flux at outlet	Tortuosity	Absolute error	Relative error
2.70E+02	0.515619	0.518655	1.2918	0.16086	0.11073
2.90E+02	0.50814	0.511943	1.3087	0.14392	0.09908
5.84E+02	0.482519	0.482914	1.3874	0.06525	0.04492
8.00E+02	0.475373	0.475344	1.4095	0.04316	0.02971
1.67E+03	0.467330	0.467329	1.4337	0.01898	0.01307
4.24E+03	0.463295	0.463297	1.4462	0.00651	0.00448
9.09E+03	0.461981	0.461982	1.4503	0.00239	0.00165
1.54E+04	0.461553	0.461553	1.4516	0.00104	0.00072
3.34E+04	0.461222	0.461222	1.4527	0.00000	0.00000
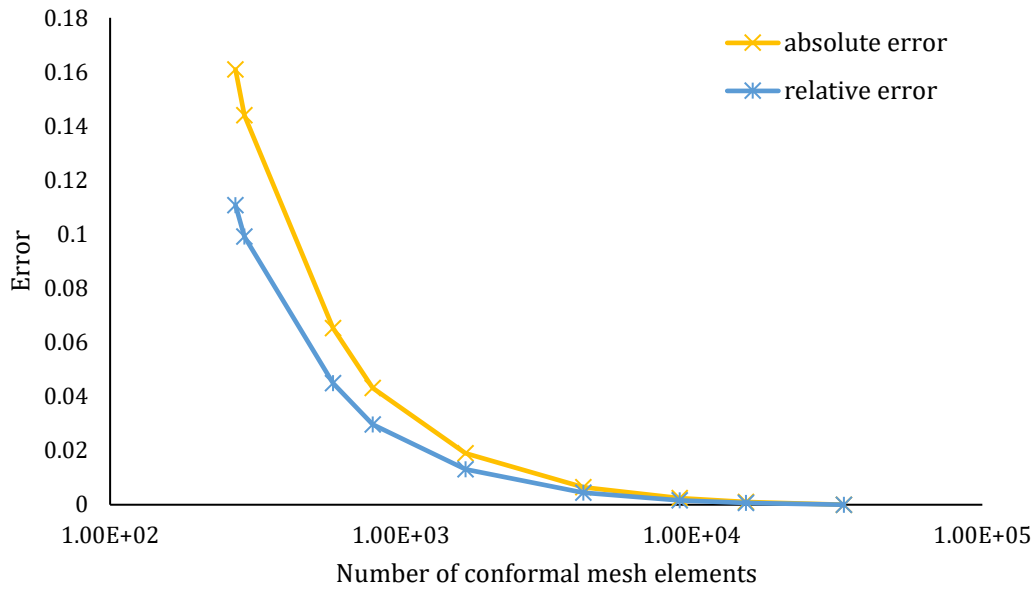
Figure 21: Reaching mesh independent reference conformal solution for porosity = 0.67

Repeating the process for geometries with porosity equal to 0.60 and 0.49 give the following values of tortuosity. Table 6 summarises the determination of tortuosity from simulation data for all images. These values are used against tortuosities from diffuse interface method to determine the method's accuracy Table 7 presents the simulation run times for mesh independent solutions with the number of mesh elements.

Table 6: Summary of tortuosity values for all three images on conformal mesh

Porosity	0.67	0.6036	0.493846
Flux $(mol/m^2 s)$	0.46122	0.39119	0.29440
Concentration inlet (mol/m^3)	1	1	1
Concentration outlet (mol/m^3)	0	0	0
D_bulk (mm^2/s)	1	1	1
Length (μm)	1000	1000	1000
D_eff (mm^2/s)	0.461222	0.391192	0.294403
Tortuosity	**1.45266**	**1.54297**	**1.67744**

Table 7: Simulation run times for tortuosity model at converged conformal meshes

Porosity	Number of mesh elements	Simulation run time (s)
0.67	15392	1.7747
0.6	14178	1.6358
0.493	12332	1.2935

3.5.2 Permeability and Inertial Constant of Porous Media

For setting up the finite element simulation for continuity equation (3.14) and Navier Stokes equation (3.15) with Dirichlet boundary conditions at *inlet*, *walls* and no stress outlet boundary condition at *outlet*, OpenCMP is used. Starting with types of finite element spaces, incompressible Navier Stokes simulation uses the standard Taylor-Hood finite element pair- VectorH1 finite element space for velocity field and H1 finite element space for pressure field. The polynomial order is set as three for velocity field and two for pressure field. Choice of solver and preconditioner are set as *direct*. The output simulation result file is saved in .vtu file format for visualization in *Paraview* – an open-source, multi-platform data analysis and visualization application [79]. Number of subdivisions in the .vtu file is set to be equal to polynomial order of the VectorH1 space that is, three. Table 8 summarises the simulation settings.

Table 8: Simulation conditions for incompressible Navier Stokes equation to determine permeability and inertial constant

Finite element space (u)	VectorH1
Finite element space (p)	H1
kinematic viscosity (mm^2/s)	1
interpolant order	3
solver	direct
preconditioner	direct
linearization method	Oseen
non-linear tolerance	1×10^{-4}
Non-linear max iterations	4
.vtu subdivisions	3

Averaged velocity magnitude and averaged pressure are measured at *inlet* and *outlet* boundaries from the simulations using *Paraview*. Varying averaged velocity and pressure magnitudes are then plotted and resulting quadratic relationship is used to

determine permeability and inertial constant. The simulation settings are kept same for simulation on a conformal mesh and a structured quadrilateral mesh with phase field for diffuse interface method. For simulations on conformal mesh, it is verified that the mesh density which gave a converged mesh independent solution for tortuosity calculation give converged mesh independent solution for pressure gradient too across domain. Results from a conformal mesh are presented as follows for reference comparison to diffuse interface method results in chapter 4.

Figure 22 shows the *Paraview* visualization of velocity magntude field for incompressible Navier Stokes model with above mentioned simulation conditions and boundary conditions on a conformal mesh as mentioned in section 3.4.2. The averaged *inlet* boundary velocity for the specific simulation is set at 0.1. As expected, the velocity magnitude can be seen rising in the areas of constriction between solids and close to zero near the solid interfaces due to no slip velocity condition at the *walls*. Figure 23 shows the variation of velocity magnitude with increasing inlet velocity. The flow becomes more convection dominated and inertial forces become more prominent than viscous forces at higher velocities.
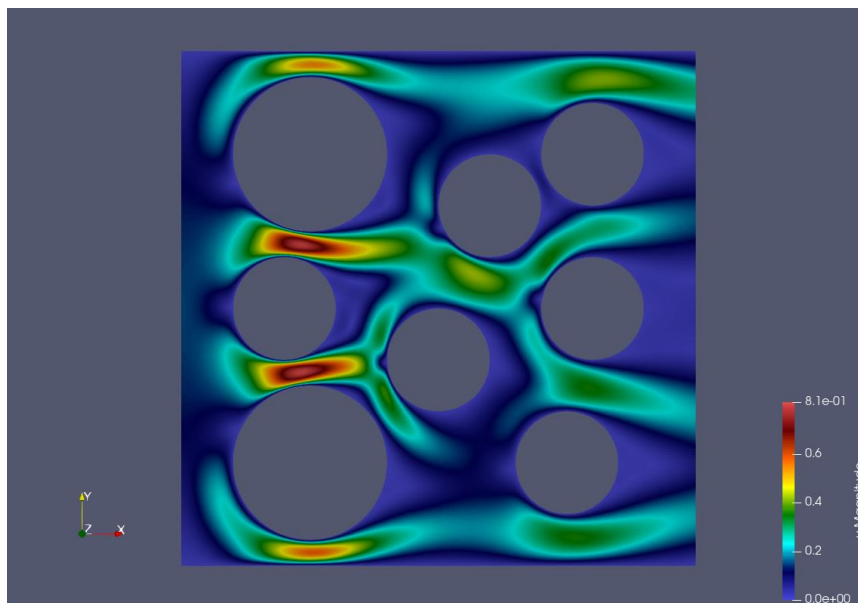
Figure 22: Velocity field visual from INS simulation on conformal mesh at inlet v =0.1
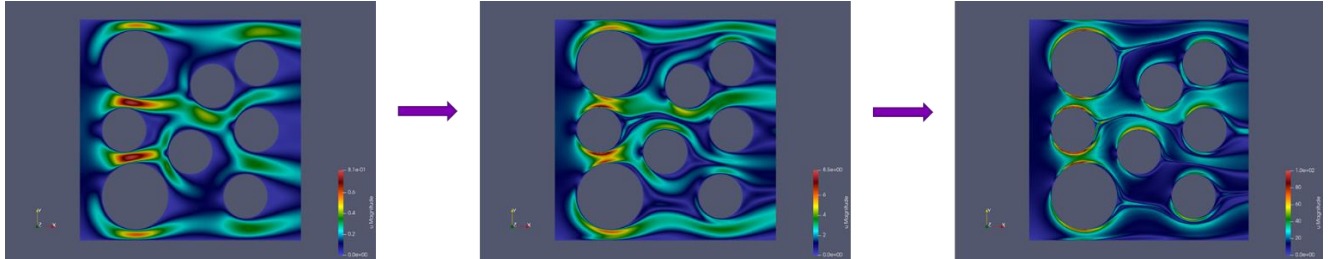
Figure 23: Velocity field visuals from INS simulation on conformal mesh at increasing inlet velocities from v = 0.1 to 10

Figure 24 and Figure 25 show the *Paraview* visualization of magnitude of velocity field at inlet velocity 0.01 and 0.1 for all the image geometries with different porosities. Due to higher constrictions and narrower pores, it can be observed that the areas of higher velocities are more prominent in image with higher porosity. It was also observed that the averaged velocity is same at *inlet* and *outlet* boundaries which is true for conservation of momentum across simulation domain.
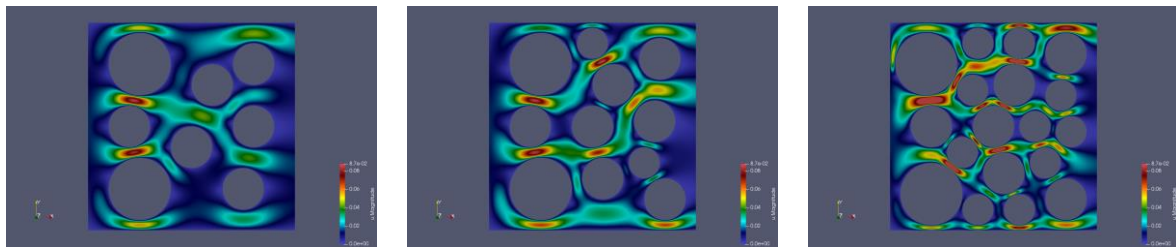
| (a) Porosity = 0.67 | (b) Porosity = 0.6 | (c) Porosity = 0.49 |

Figure 24: Reference conformal mesh velocity field visuals for three different geometries with varying porosities at inlet v = 0.01
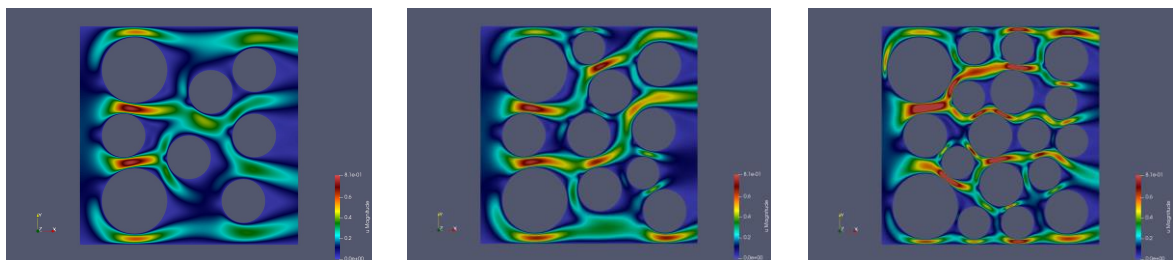
| (a) Porosity = 0.67 | (b) Porosity = 0.6 | (c) Porosity = 0.49 |

Figure 25: Reference conformal mesh velocity field visuals for three different geometries with varying porosities at inlet v = 0.1

Simulations are conducted on the conformal meshes of three images with varying inlet velocities. The pressure gradient is measured for each simulation and plotted against each averaged inlet velocity. Figure 26 shows the three Forchheimer plots for all three images. The quadratic correlation between pressure gradient and velocity determined from the plots can be then compared with Forchheimer equation (3.11) to obtain the coefficients. It can also be observed that permeability decreases and inertial constant increases with decreasing porosity which holds true for experimental observations [80].

Table 9 presents the simulation run times for mesh independent solutions at inlet velocity of 0.1 with the number of mesh elements. The simulation run times are similar in the velocity bracket of $0.5 - 0.15$ for which permeability and inertial constant are determined for a given porosity.

Table 9: Simulation run times for incompressible Navier Stokes model at converged conformal meshes

Porosity	Number of mesh elements	Simulation run time (s)
0.67	15392	16.9248
0.6	14178	14.5709
0.493	12332	11.5104

(a)

(b)

56

$$dp/dx = 0.03119v^2 + 0.02186v$$
$$R^2 = 0.99996$$
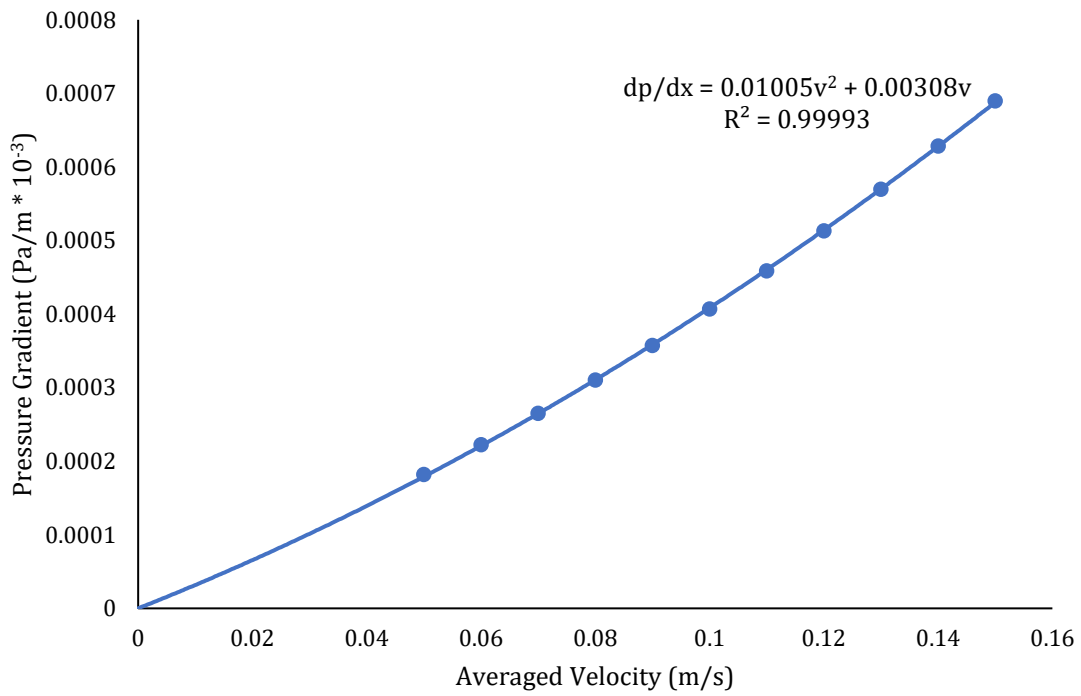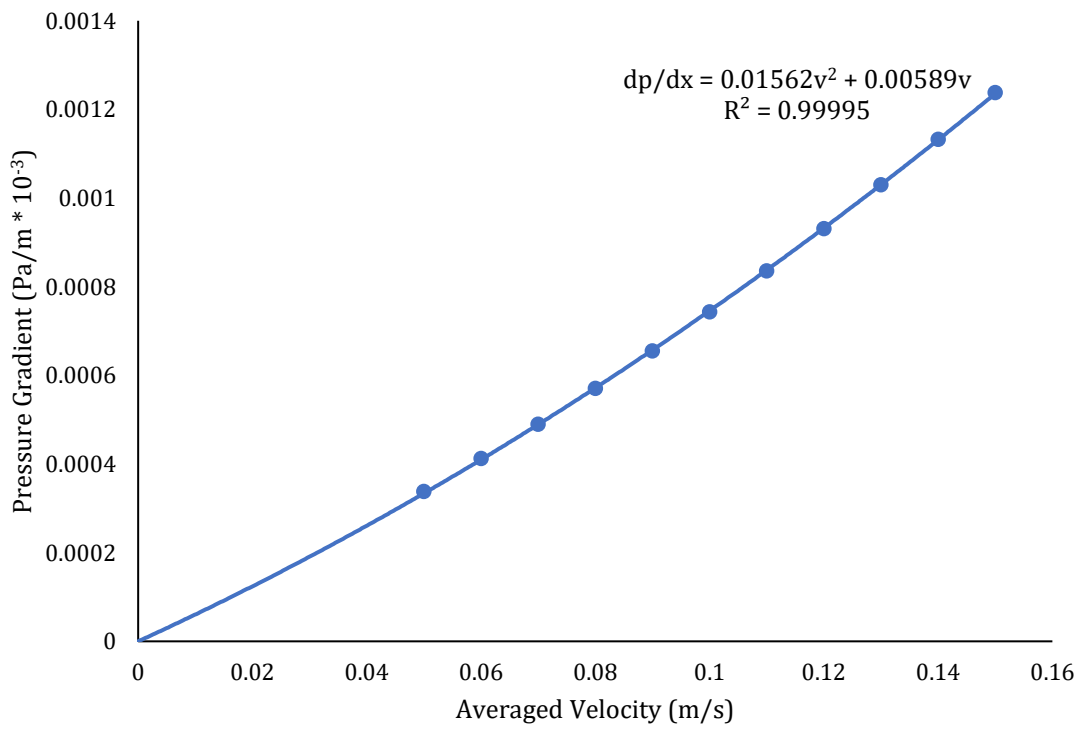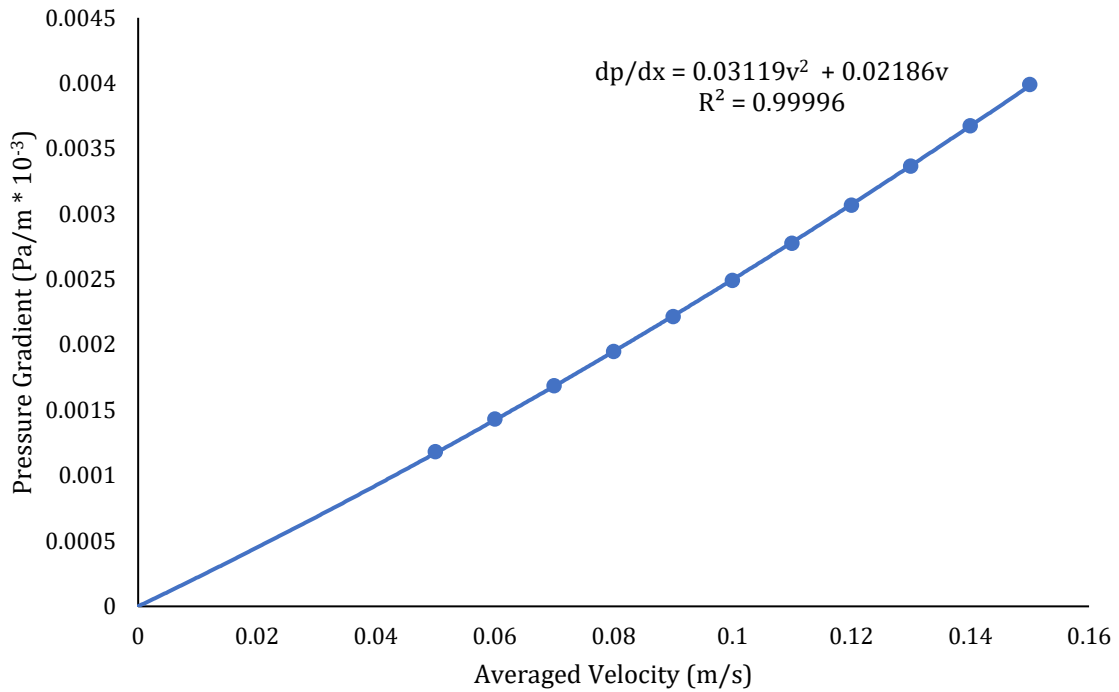
(c)

Figure 26: Reference conformal mesh Forchheimer curves for three different porous media geometries with varying porosities

The following values of permeability and inertial constant presented in Table 10 are determined from the plots in Figure 26 and are used in section 4.2 for comparison to simulation results from diffuse interface method.

Table 10: Summary of fluid flow properties for all three images on conformal mesh

Porosity	Permeability ($10^{-6} \times m^2$)	Inertial constant (m^{-1})
0.67	324.8335	0.0100495
0.6	169.6669	0.0156207
0.493	45.7411	0.0311932

4 RESULTS AND DISCUSSION

This chapter discusses the determination of tortuosity, permeability, and inertial constant from mass diffusion and incompressible Navier Stokes models implemented using diffuse interface method. The chapter is divided into two sections, one for determination of tortuosity and other for determination of permeability and inertial constant using diffuse interface method. Figure 27 and Figure 28 show examples of phase field and gradient of phase field projected onto a structured quadrilateral mesh with coarseness ratio ten and DI width one. Simulations were run on these phase fields and structured mesh with varying parameters as identified in section 3.3. These diffuse interface parameters are analysed, and simulations are run with varying parameters to reach ideal combinations with reasonable accuracy compared to conformal mesh results and low simulation run time.
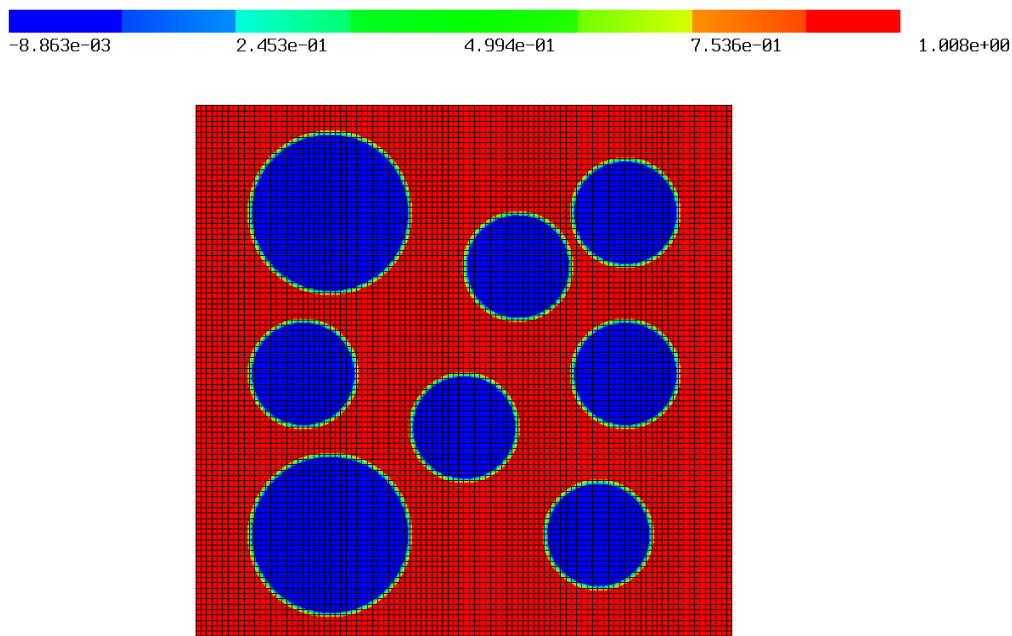
Figure 27: Example of phase field projected onto a structured quadrilateral mesh with coarseness ratio = 10 and DI width = 1
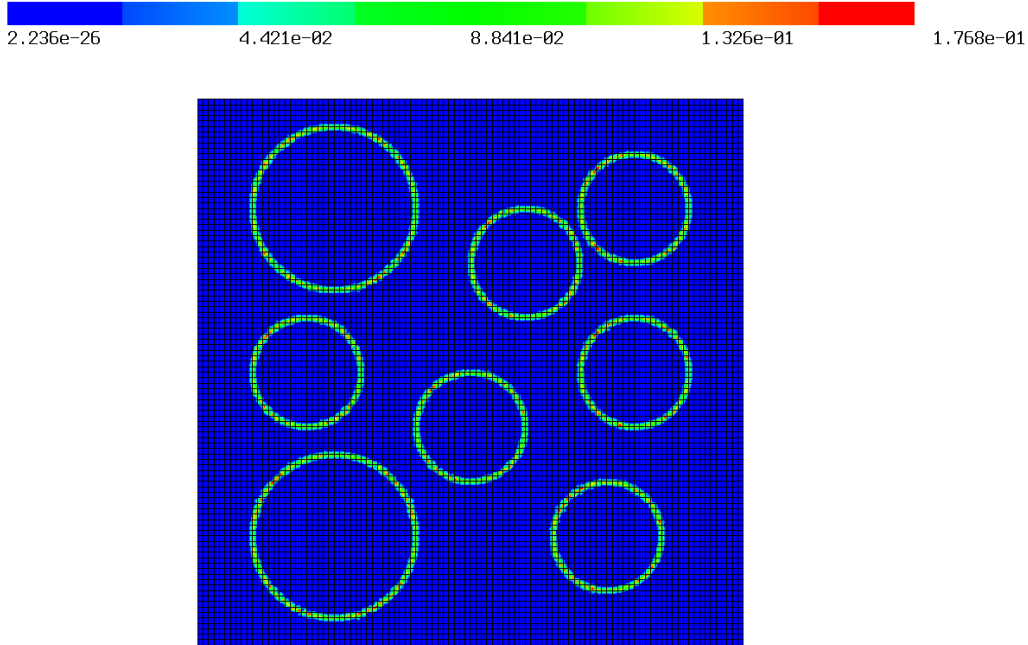
Figure 28: Example of gradient of phase field projected onto a structured quadrilateral mesh with coarseness ratio = 10 and DI width = 1

4.1 Tortuosity of Porous Media using DI Method and comparison

For modelling mass diffusion to determine tortuosity using diffuse interface method, firstly the phase field representing porous media is generated with varying diffuse interface width. Then, the phase field ϕ and gradient of phase field $|\phi|$ is projected onto a structured quadrilateral mesh with varying mesh scale hence varying coarseness ratio. The coarseness ratio is varied from one to ten. Since the image resolution is 1000×1000 as described in section 3.1, the structured quadrilateral mesh scale varies from 1000×1000 to 100×100. The diffuse interface width has been set to vary from ten mesh elements to one mesh element of the structured mesh. The tortuosity model as formulated in section 3.4.1 is simulated in this section.

For conducting the diffuse interface finite element simulation for Poisson equation (3.8) with Dirichlet boundaries at *inlet* and *outlet* and Neumann boundaries at *walls*, OpenCMP is used. Similarly as finite element method on conformal mesh, Poisson simulation uses standard H1 finite element space for scalar variable with polynomial order equal to three. Choice of solver and preconditioner are set as *direct*. The output simulation result file is saved in .vtu format for visualization in *Paraview*. Number of subdivisions in the .vtu file is set to be equal to polynomial order of the H1 space that is, three.

Table 11: Simulation conditions for Poisson equation to determine Tortuosity

Finite element space	H1
interpolant order	3
DIM penalty coefficient	10
solver	direct
preconditioner	direct
.vtu subdivisions	3

Mass flux is measured at *inlet* and *outlet* boundaries from the simulations using *Paraview*. The mass flux determined from simulations is then substituted into equation (3.10) to determine tortuosity. Results from a structured quadrilateral mesh with diffuse interface method are presented as follows. Figure 29 and Figure 30 show example of simulation results for concentration field and magnitude of concentration gradient field for coarseness ratio of one and diffuse interface width of one mesh element for image with porosity 0.67. It can be observed that in the areas of simulation domain where phase field is zero (inside solid domain), the concentration and concentration gradient fields are zero.
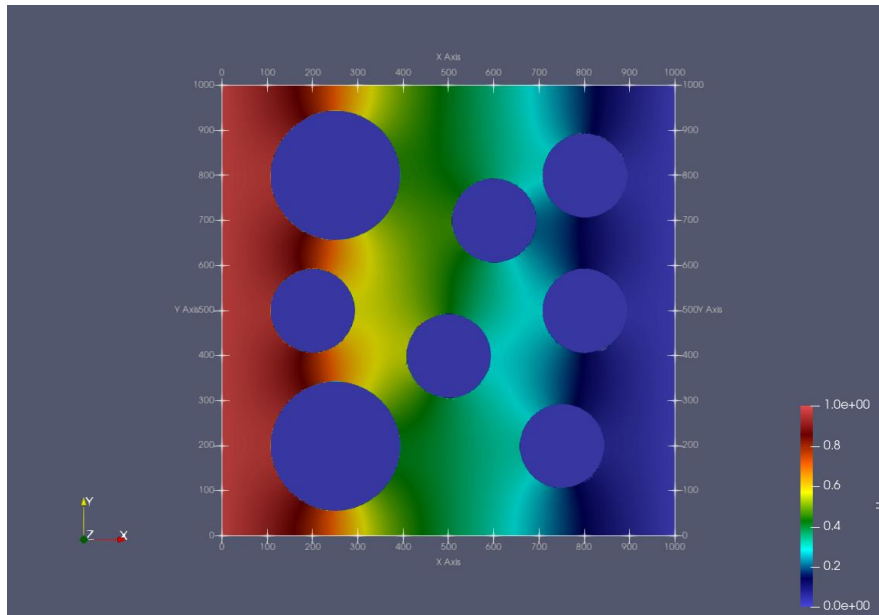
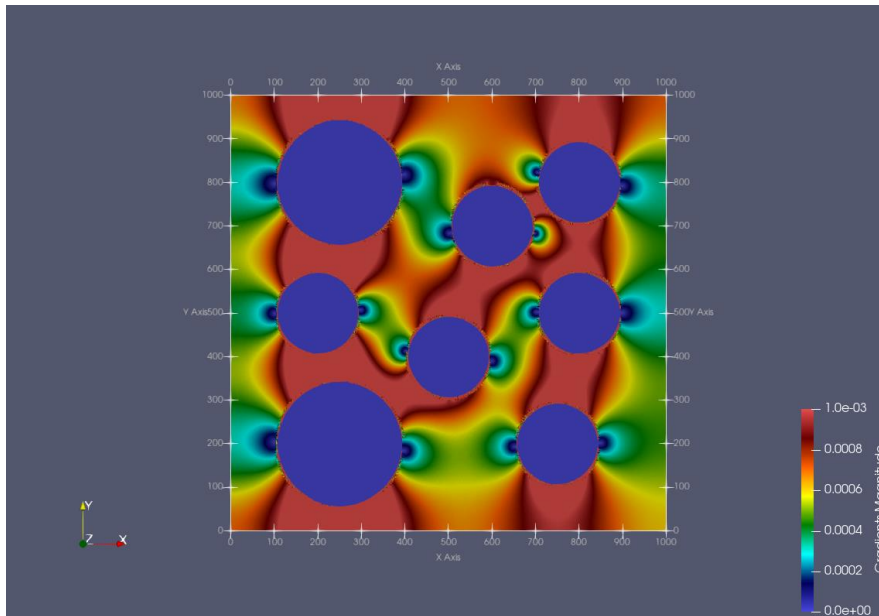**Figure 29: Concentration field visual from simulation using diffuse interface method**

Figure 30: Concentration gradient field visual from simulation using diffuse interface method

For comparison to conformal mesh results, the numerical values of tortuosity (τ) obtained from varying parameters are compared to converged conformal mesh solution. The relative error is defined in equation (4.1).

$$relative\ error = \frac{\tau_{DIM} - \tau_{conformal\ mesh}}{\tau_{conformal\ mesh}} \qquad \textbf{(4.1)}$$

Simulations with varying parameters are done on image with porosity 0.67 and ideal parameters are determined. Then, tortuosity at ideal parameters is determined for other images with different porosities. Figure 31 shows the variation of relative error with different parameters. First observation can be made that the relative error decreases with diffuse interface (DI) width. Large values of DI width extend the Neumann boundary condition constraints into the interior of the solid boundary thereby reducing accuracy. Secondly, it can be observed that the error is significantly more for higher coarseness ratio or more coarse mesh at high DI width. Decreasing coarseness ratio increases the accuracy of the solution by increasing the order of the spatial approximation. At coarseness ratio of ten, the error reduces by two orders of magnitude from diffuse interface width of ten to one whereas the drop in error for coarseness ratio of one is not so drastic. Most importantly, it is observed that at DI width of one, the relative error is lowest for all coarseness ratios and determined to be 2.52×10^{-3} for coarseness ratio of ten. In the work by Monte et al. [11] where Poisson equation was simulated using diffuse interface method it was also presented that the highest accuracy was observed when DI width was equal to one mesh element. Table 12 shows the time taken for different mesh coarseness ratios. The time taken is lowest for highest coarseness ratio which is obvious because of lower number of elements. Low run time makes the simulation feasible for determining property of porous media image, in this case tortuosity. It is also observed that the simulation run time for DIM is more compared to FEM on conformal meshes at similar number of mesh elements.
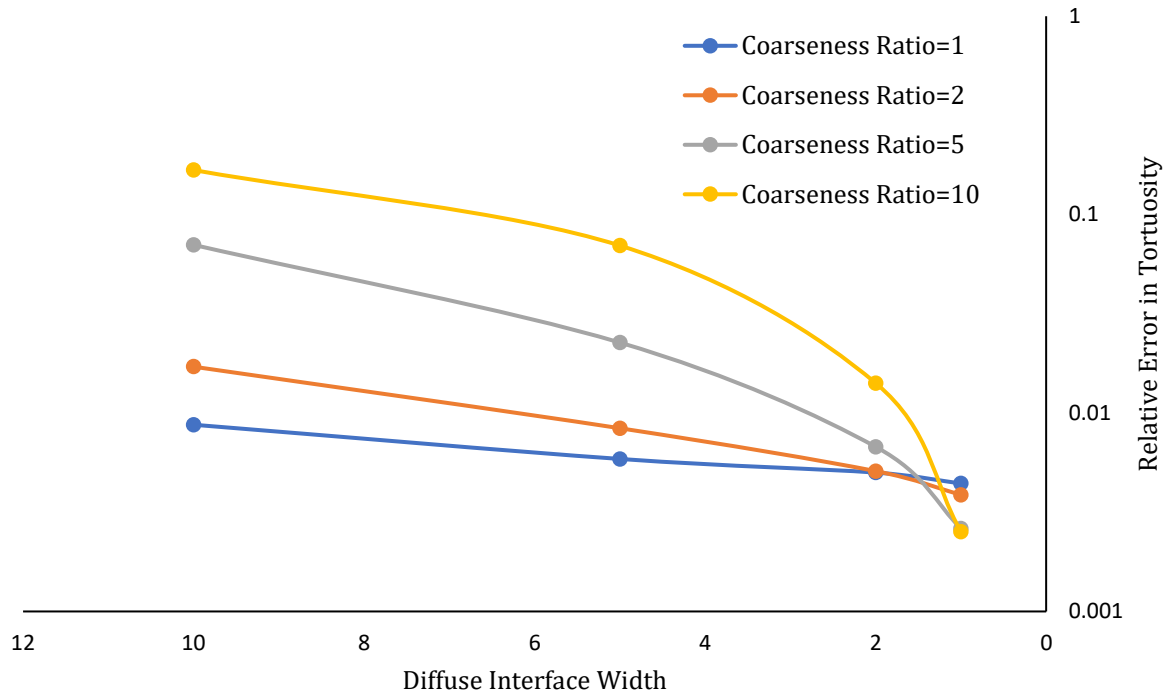
Figure 31: Comprehensive error comparison in tortuosity for varying DIM parameters

Table 12: Simulation run times for tortuosity model at varying coarseness ratios using DIM at DI width = 1

Coarseness Ratio	Number of mesh elements	Run time (s)
10	10000	3.578058
5	40000	12.28338
2	250000	86.43931
1	1000000	2601.533

On basis of these findings, tortuosity is determined for images with porosity 0.60 and 0.49 at DI width of one and coarseness ratio of ten. The tortuosity values are compared to that from conformal mesh and presented as follows in Table 13. In conclusion, relative error in tortuosity less than 0.75% is achieved for all three images.

Table 13: Summary of tortuosity results from DIM and relative error compared to conformal mesh results

Porosity	Tortuosity	Relative error
0.67	1.448999542	0.002519831
0.6	1.550100926	0.004621558
0.493	1.689870277	0.007410266

4.2 Permeability and Inertial Constant of Porous Media using DI Method

For modelling incompressible Navier Stokes fluid flow to determine permeability and inertial constant using diffuse interface method, firstly the phase field representing porous media is generated with varying diffuse interface width. Then, the phase field ϕ and gradient of phase field $|\phi|$ is projected onto a structured quadrilateral mesh with varying mesh scale hence varying coarseness ratio. The coarseness ratio is varied from five to twenty. Since the image resolution is 1000×1000 as described in section 3.1, the structured quadrilateral mesh scale varies from 200×200 to 50×50. The diffuse interface width has been set to vary from three mesh elements to one mesh element of the structured mesh. The fluid flow model as formulated in section 3.4.2 is simulated in this section.

OpenCMP is used to set up the finite element simulation for continuity equation (3.14) and Navier Stokes equation (3.15) with Dirichlet boundary conditions at $inlet, walls$ and no stress outlet boundary condition at $outlet$. The simulations settings are similar to those applied with conformal mesh. Incompressible Navier Stokes simulation uses the standard Taylor-Hood finite element pair- VectorH1 finite element space for velocity field and H1 finite element space for pressure field. The polynomial order is set as three for velocity field and two for pressure field. Choice of solver and preconditioner are set as $direct$. The output simulation result file is saved in .vtu file format for visualization in $Paraview$. Number of subdivisions in the .vtu file is set to be equal to polynomial order of the VectorH1 space that is, three. Averaged velocity magnitude and averaged pressure are measured at $inlet$ and $outlet$ boundaries from the simulations using $Paraview$. Varying averaged velocity and pressure gradient magnitudes are then plotted and resulting quadratic relationship is used to determine permeability and inertial constant.

Table 14: Simulation conditions for incompressible Navier Stokes equation to determine permeability and inertial constant

|	
Finite element space (u)	VectorH1
Finite element space (p)	H1
kinematic viscosity (mm^2/s)	1
interpolant order	3
DIM penalty coefficient	10
solver	direct
preconditioner	direct
linearization method	Oseen
non-linear tolerance	1×10^{-4}
Non-linear max iterations	4
.vtu subdivisions	3

4.2.1 Isomorphic Transformation

Since it was observed in section 4.1 that the relative error was minimum at diffuse interface width of one mesh element, the incompressible Navier Stokes equation at inlet velocity of 0.01 was firstly simulated at DI width of one and presure gradient determined from simulation was compared to results from conformal mesh. As shown in Figure 32, the pressure gradient observed from simulation is very different compared to that from conformal mesh. On closer observation, it can be seen that the spacing between solids is reduced leading to more constricted pore spaces. It was then hypothesized that there is a 'swelling' phenomenon on the solid bodies because of adding diffuse interface width with Dirichlet boundary condition on interface which is leading to higher pressure gradients. No slip boundary condition i.e., zero velocity at solid interface imposes zero velocity on the entirety of diffuse interface. This error in velocity field at the solid interface was also observed in the work of Stoter et al. where diffuse interface method was applied on Navier Stokes equations for perfusion profile of a human liver MRI scan [13]. Discrepancy in pressure drop can also be explained by Hagen Poisseuille equation

(4.2) where pressure drop is inversely proportional to the fourth power of fluid flow path radius and constricted pores means lower radius and higher pressure drop.

$$\nabla p = \frac{8\mu Q}{\pi R^4} \qquad \textbf{(4.2)}$$

where Q is volumetric flow rate and R is radius of flow path.
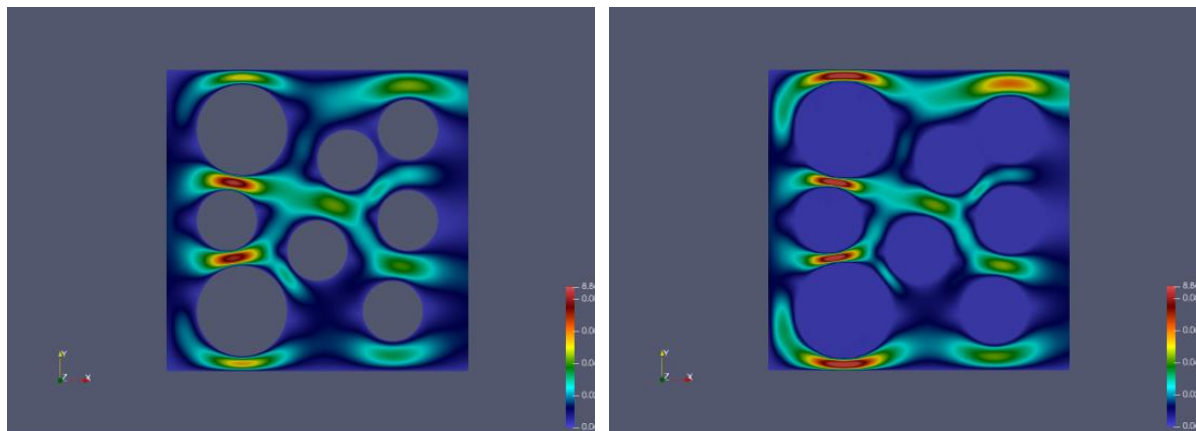
Pressure Gradient = 3.46×10^{-5} Pressure Gradient = 8.58×10^{-5}

(a) Conformal mesh simulation at inlet v=0.01

(b) DIM simulation at inlet v=0.01, coarseness ratio=10 and DI width=1

Figure 32: Comparison of INS simulation pressure gradient results using diffuse interface method with conformal mesh results at inlet velocity = 0.01

To obtain reasonable accuracy in pressure gradient, it's important to perform simulations on phase fields of porous media with correct approximation of expanse of solid domain. To mitigate this 'swelling' effect due to added diffuse interface, isomorphic transformation is performed on the phase field and expanse of solid domain is corrected to match original size. Isomorphic transformation means changing the size of solid bodies within NumPy array of phase field while preserving the shape of the solids. Since porous media solid geometries are very irregular with varying features, a simple image erosion can not be performed on the solid interface. Image erosion can change the image morphology. Isomorphic transformation is demonstrated in Figure 33 by an example of an image of square. Image geometry is chosen as square to make sure that the image

67

features like sharp corners are not lost after the transformation. The size of the solids at the interface is reduced by the number of pixels equal to added diffuse interface width. This is done by taking a Euclidean distance transform on NumPy image array using python *edt* package [77]. Then, the part of the image where value of distance transform is less than λ is set to binary value of zero. Since, in the image shown in Figure 33 (a) binary value of one indicates solid and zero indicates pore space. Now that the image is obtained with reduced solid size, same procedure is followed as discussed in section 3.2.2 to get a phase field ϕ. Images in Figure 33(d) and Figure 33 (a) are compared and it's verified that the expanse of phase field with diffuse interface is same as the original size of solid square.
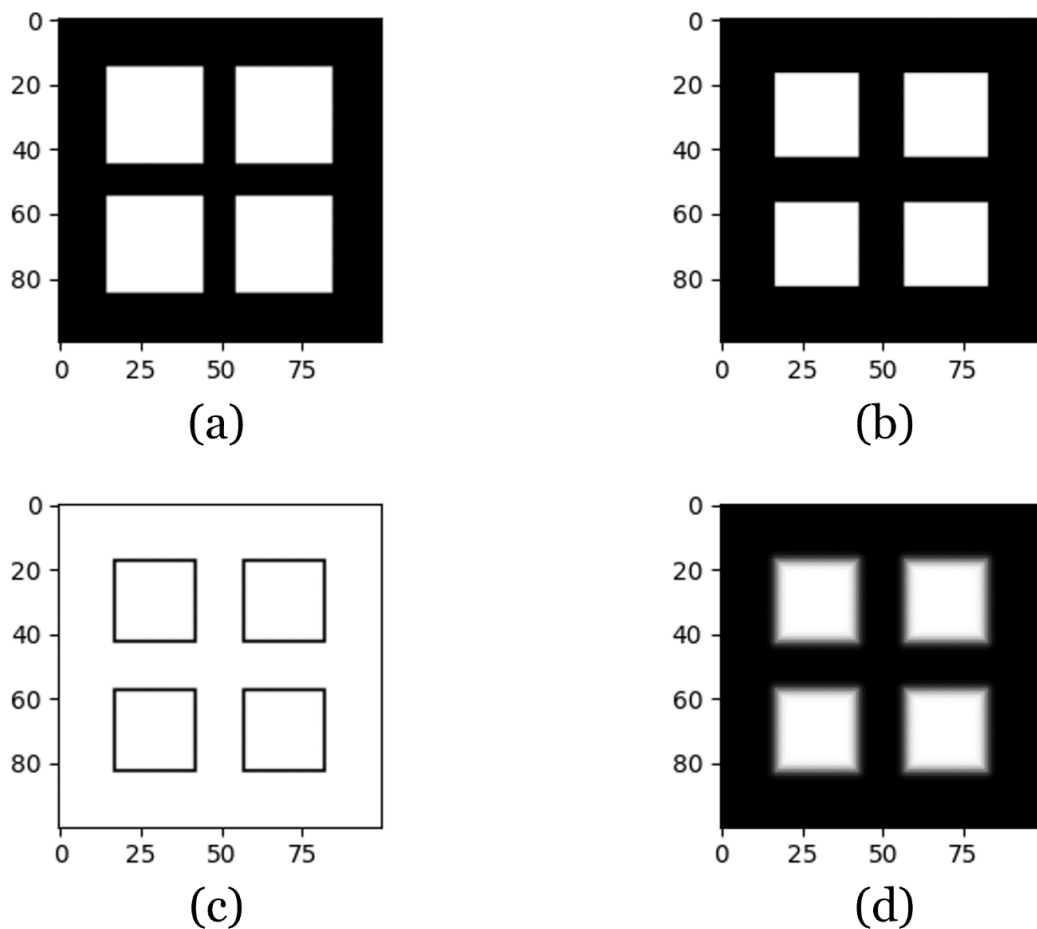

Figure 33: Isomorphic Transformation demonstrated through (a) original image (b) image with reduced size of solids (c) solid border extracted by image erosion and (d) final phase field with solid expanse matching original image

Now that expanse of solids is corrected by isomorphic transformation, incompressible Navier- Stokes simulations can be performed on this image and pressure gradient can be determined. Section 4.2.2 discusses these simulations and the ideal diffuse interface method parameters obtained from simulations.

4.2.2 Ideal Diffuse Interface Method Parameters

For comparison to conformal mesh results, the magnitude of pressure gradient obtained from varying parameters is compared to converged conformal mesh solution. The relative error is defined in equation (4.1).
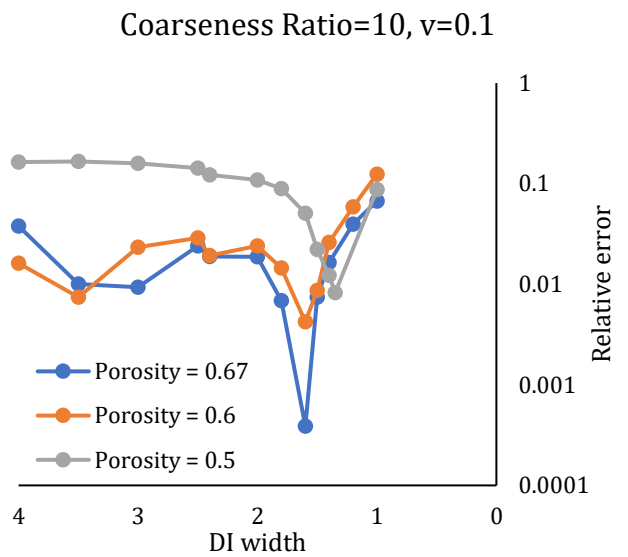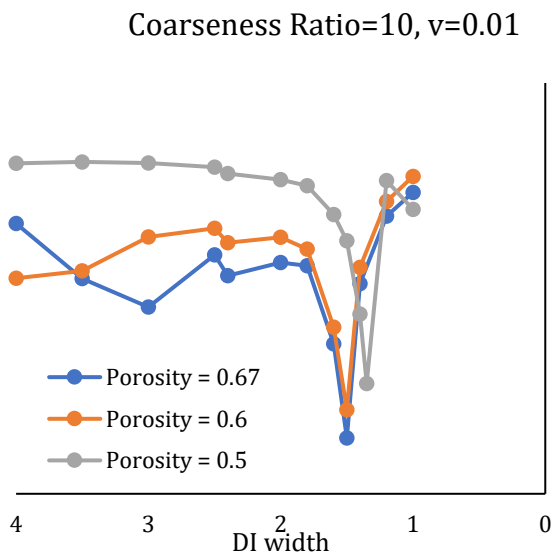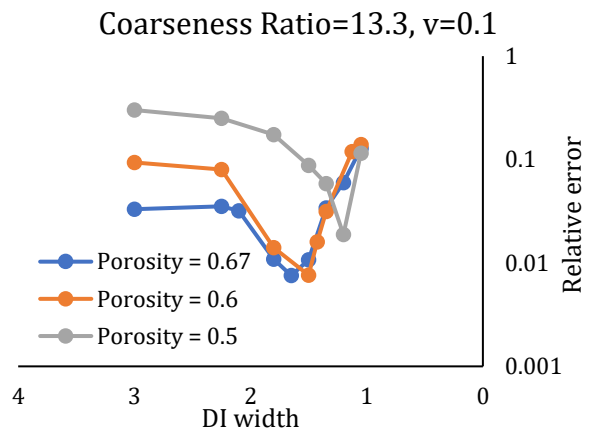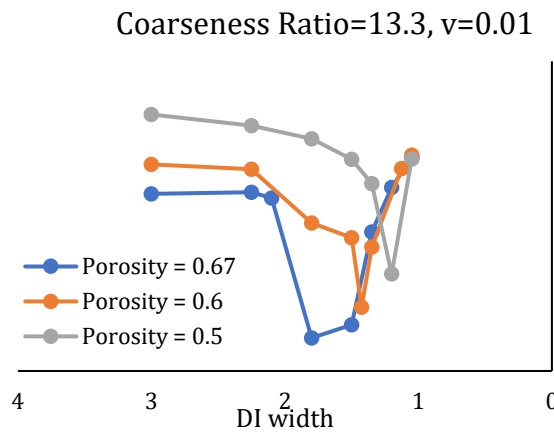
$$relative\ error = \frac{\nabla p_{DIM} - \nabla p_{ref}}{\nabla p_{ref}} \qquad \textbf{(4.3)}$$

where ∇p_{DIM} is the magnitude of pressure gradient determined from diffuse interface method and ∇p_{ref} is the reference magnitude of pressure gradient determined from simulation on conformal mesh.

Incompressible Navier Stokes model as formulated in section 3.4.2 with varying DIM parameters is simulated on the three images and ideal parameters are determined. Figure 34 presents comprehensive summary of variation of relative error with different coarseness ratios, porosities, and diffuse interface (DI) width. The parametric analysis is done on three separate images to make sure that the ideal parameters determined are consistent with multiple images. The coarseness ratio is varied from twenty to five i.e., the mesh scale varies from 50×50 to 200×200. The DI width varies from three mesh elements to one mesh element of the structured mesh. The parametric analysis is done at two different inlet velocities to ensure that determined ideal parameters are consistent with changing velocities.

Many key conclusions have been drawn out from Figure 34. Firstly, and most importantly, the ideal DI width is determined from the plots for each coarseness ratio where relative error in pressure gradient is minimum. For all set of simulations at each porosity, it is observed that the ideal DI width lies in the bracket of $1 - 2$ mesh elements where relative error drops at least below 1%. Though, the relative error is sensitive around this bracket,

it varies between 1% to 10%. It is also observed that at coarseness ratio of 5 when the mesh density is finest, the minimum relative error is found at DI width of 1. Secondly, at any given DI width for all the plots, relative error is higher at higher porosity. This is because of the higher surface area of solid interface leading to more mesh elements with diffuse interface. As found in the work of Stoter et al [13], the increase in relative error can largely be attributed to a localized increase in error at the interface. This localized error does not visibly affect the velocity and pressure field solution away from the interface. It's also observed that there is some correlation between ideal DI width and porosity. Ideal DI width for each coarseness ratio and velocity is shifted to the right by a small margin for decreasing porosity or increasing diffuse interface mesh elements. Lastly, it is observed that at higher coarseness ratio the relative error at ideal DI width is comparable to lower coarseness ratios. Hence, simulations can be done at very coarse meshes (50×50) to determine pressure gradient across the domain from simulations and macroscale properties- permeability and inertial constant can be calculated accurately.

Coarseness Ratio=20, v=0.01

Coarseness Ratio=20, v=0.1

Coarseness Ratio=13.3, v=0.01

Coarseness Ratio=13.3, v=0.1

Coarseness Ratio=10, v=0.01

Coarseness Ratio=10, v=0.1

71
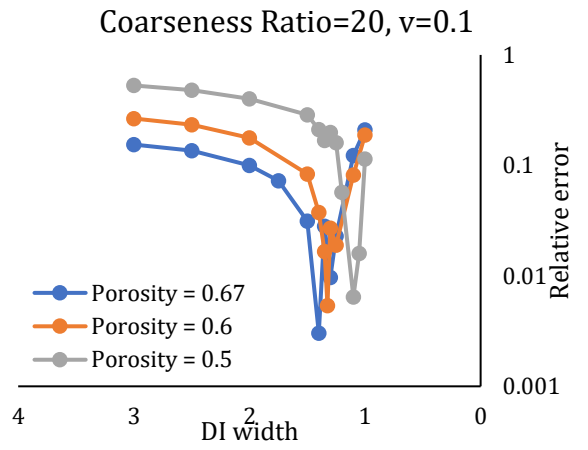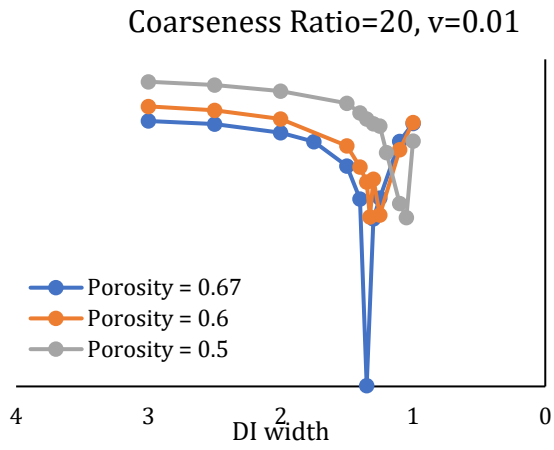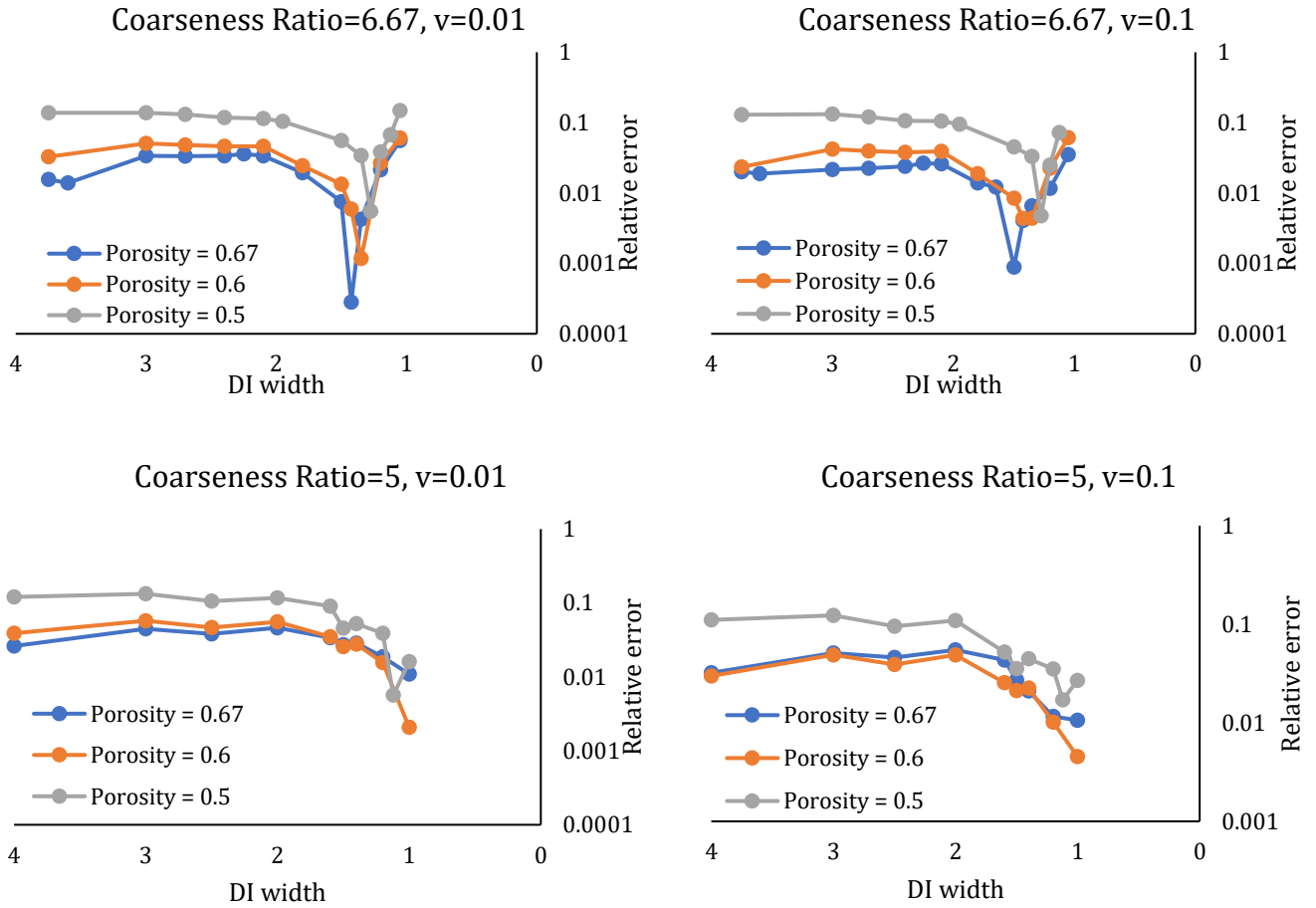
Figure 34: Comprehensive Coarseness Ratio vs DI width comparison for varying porosity, coarseness ratio, DI width and velocities

4.2.3 Comparison of Results between DI Method and Conformal Meshing

Figure 35 and Figure 36 show the *Paraview* visualization of magnitude of velocity field at inlet velocity 0.01 and 0.1 for incompressible Navier Stokes model with isomorphic transformation on phase field, mentioned simulation and boundary conditions for all the porous media images with different porosities. The velocity field visuals and the spacing between solids is similar to those presented in section 3.4.2 It was also verified that the averaged velocity is same at *inlet* and *outlet* boundaries which is true for conservation of momentum across simulation domain.
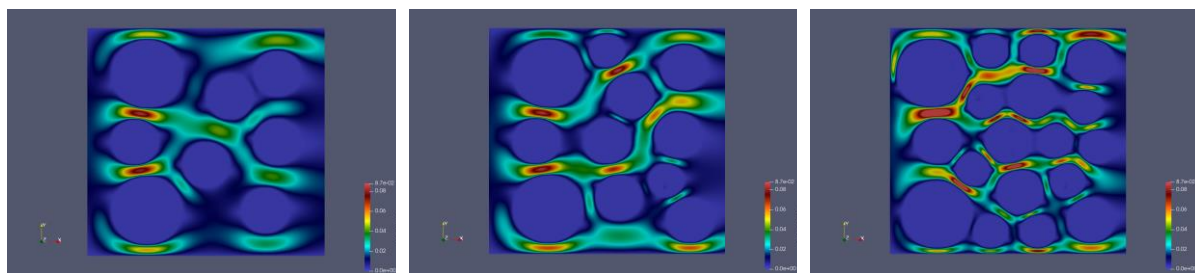
(a) Porosity =0.67   (b) Porosity =0.60   (c) Porosity =0.49

Figure 35: DIM simulations velocity field visuals for three different geometries with varying porosities at inlet v = 0.01
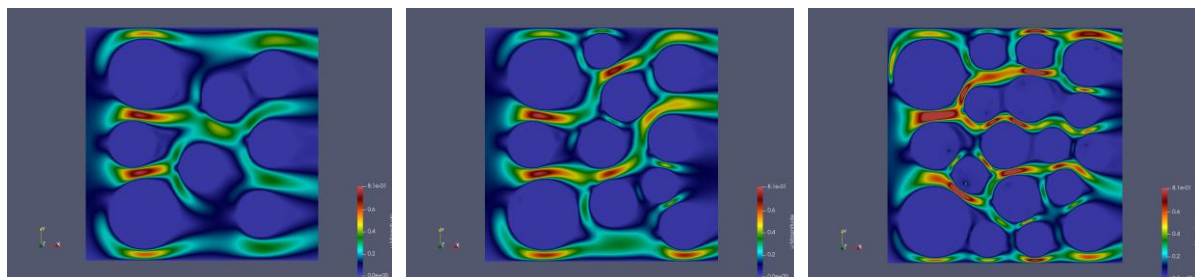
(a) Porosity =0.67   (b) Porosity =0.60   (c) Porosity =0.49

Figure 36: DIM simulations velocity field visuals for three different geometries with varying porosities at inlet v =0.1

Simulations are conducted on the structured meshes of three images with varying inlet velocities. The pressure gradient is measured for each simulation and plotted against each averaged inlet velocity. The simulations done on conformal mesh were stable and converging for increasing velocities but that was not observed with DIM. At inlet velocities greater than 0.1, the simulations diverged at coarseness ratio of ten or above (mesh scale 100×100 and coarser). And at inlet velocities above 0.15, the simulations diverged at coarseness ratio of 6.67 or above(mesh scale 150×150 and coarser). So, to be consistent with mesh scale throughout all velocity simulations, the velocity range is determined above which the quadratic behaviour between pressure gradient and averaged velocity does not change. The velocity range of 0.05 – 0.15 was determined for getting converged quadratic relationship. The mesh scale of 150×150 is chosen for all simulations since it is the coarsest mesh scale at which simulations with inlet velocity 0.15 and lower are stable and converging. For coarseness ratio of 6.67 (mesh scale of 150×150), the ideal DI width is taken from Figure 34 for each porosity- 1.5 for image porosity 0.67, 1.35 for image porosity 0.60 and 1.27 for image porosity 0.49. Now that ideal parameters are found, the simulations are performed at varying inlet velocities and pressure gradient versus inlet velocity graphs are plotted. Figure 37, Figure 38 and Figure 39 present the three Forchheimer plots for all three images using (a) conformal mesh and (b) diffuse interface method. The quadratic relationship between pressure gradient and velocity determined from the plots are then compared with Forchheimer equation (3.11) to obtain the coefficients. Table 15 presents the numerical values of constants and the relative error compared to those from finite element method on conformal meshes. In conclusion, relative error in permeability less than 1% and relative error in inertial constant less than 3% is achieved for all three images.
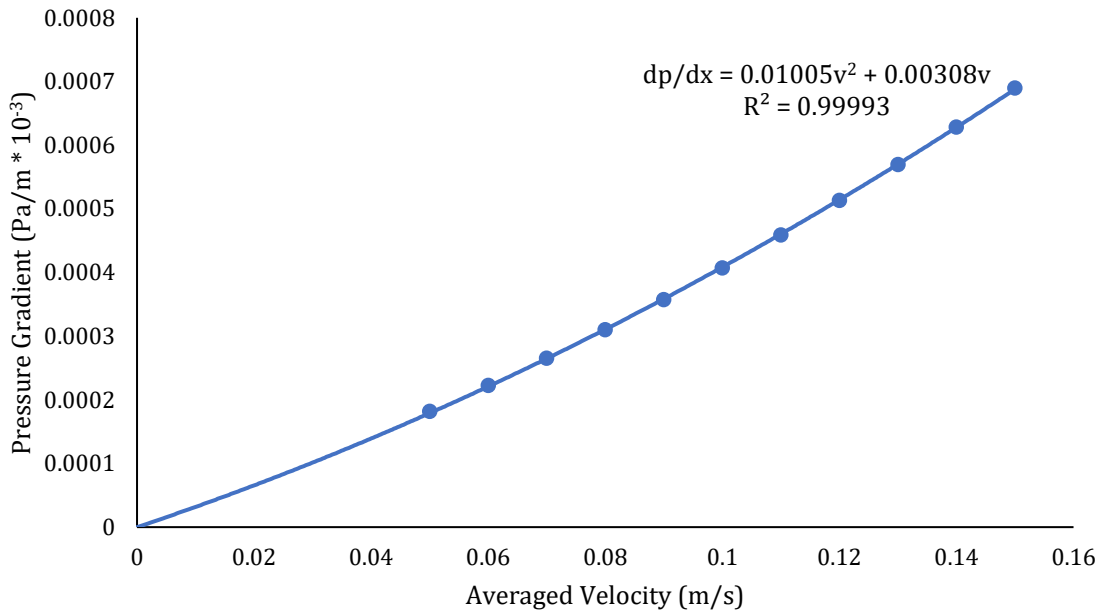
(a) Conformal Mesh Forchheimer curve for Porosity = 0.67
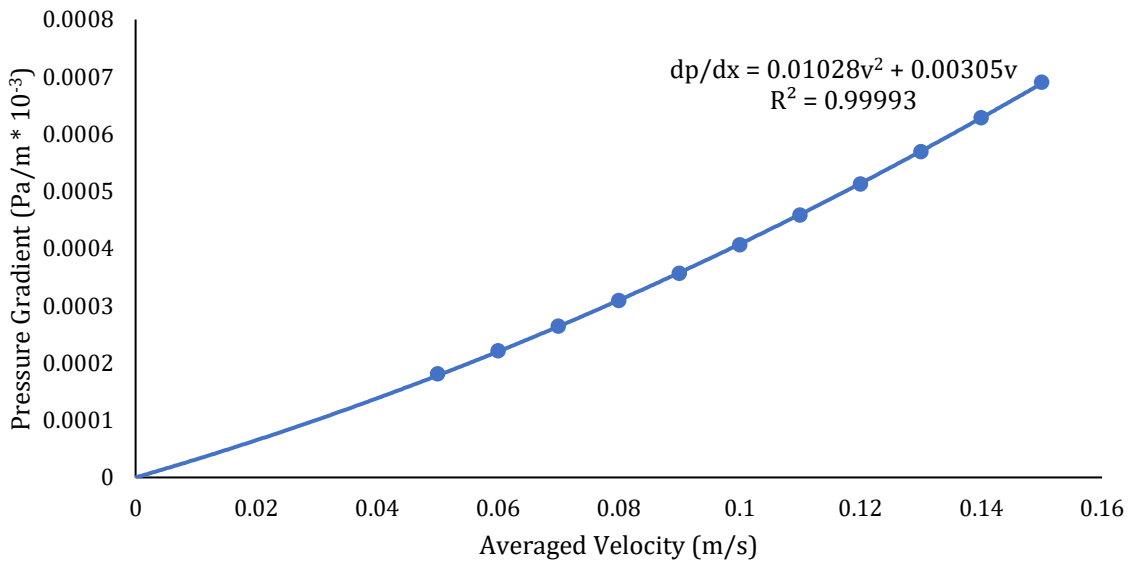
(b) Diffuse Interface Method Forchheimer curve for Porosity = 0.67

Figure 37: Forchheimer regime curve comparison at ideal parameters for Porosity=0.67

(a) Conformal Mesh Forchheimer curve for Porosity = 0.60

(b) Diffuse Interface Method Forchheimer curve for Porosity = 0.60

Figure 38: Forchheimer regime curve comparison at ideal parameters for Porosity=0.60
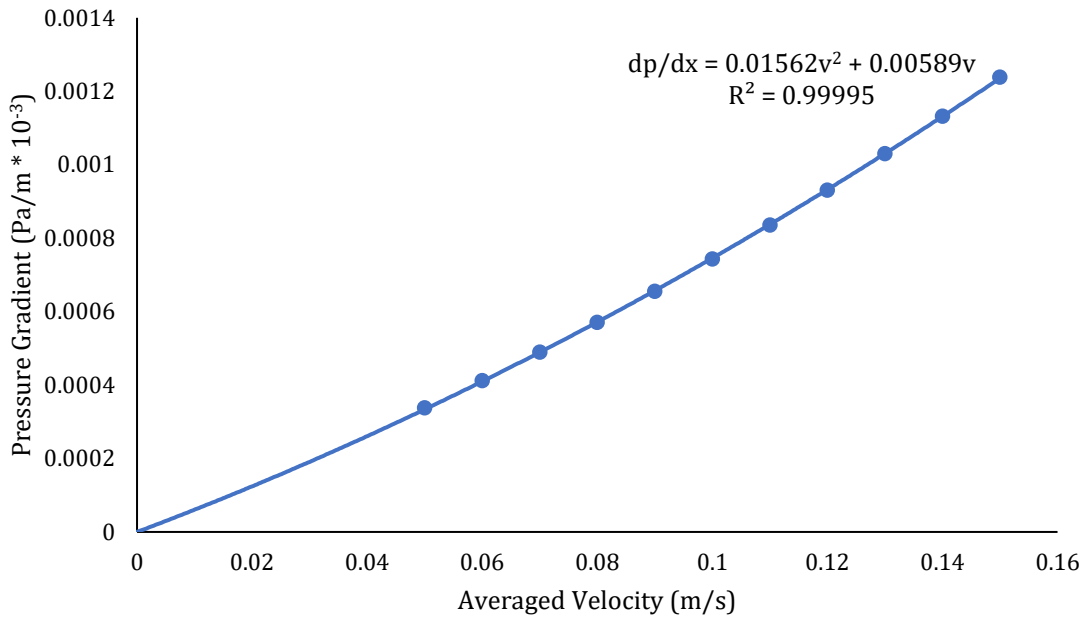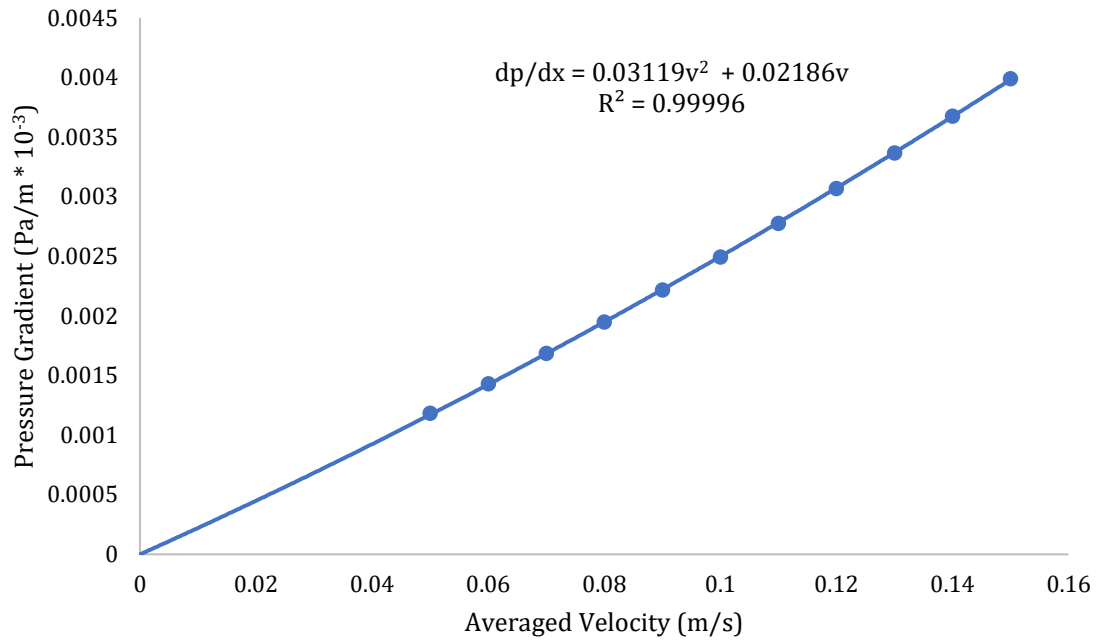
(a) Conformal Mesh Forchheimer curve for Porosity = 0.49
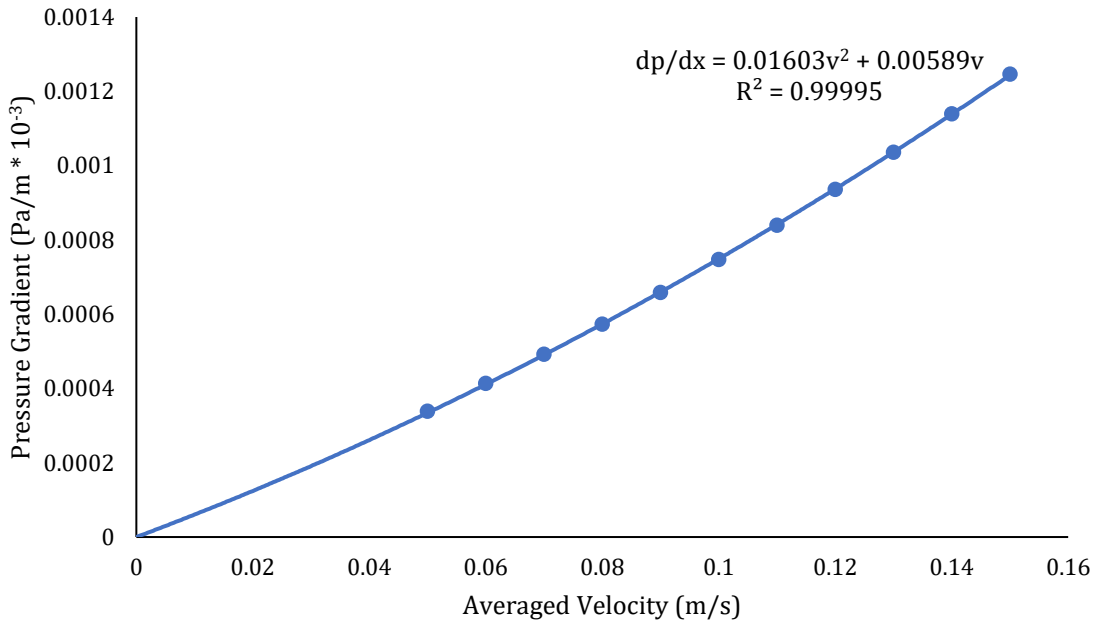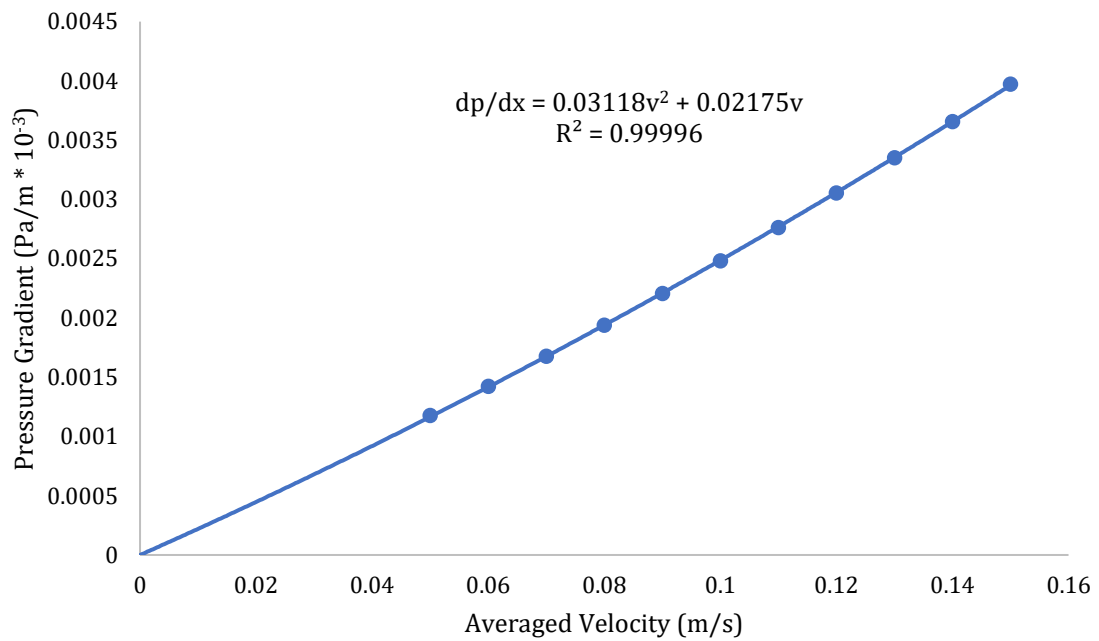

(b) Diffuse Interface Method Forchheimer curve for Porosity = 0.49

Figure 39: Forchheimer regime curve comparison at ideal parameters for Porosity=0.49

Table 15: Summary of fluid flow constants from DIM and relative error compared to conformal mesh results

Porosity	Permeability $(10^{-6} \times m^2)$	Inertial constant (m^{-1})	K relative error	β relative error
0.67	328.0732	0.0102751	0.009973426	0.022448878
0.6	169.8802	0.0160283	0.001257114	0.026093581
0.493	45.9869	0.0311824	0.005375874	0.000346229

Table 16 and Table 17 present the simulation run times using DIM on the three images at coarseness ratio of 10 and 6.67 respectively at inlet velocity of 0.1. The run times are similar for a given porosity and coarseness ratio between DI width of 1 to 2. These simulation times are considerably more compared to those on conformal meshes as shown in Table 9. Thus encouraging the need for optimised fluid flow solvers for DIM on structured quadrilateral meshes. It is also observed that the run times decrease with decreasing porosity because of the lesser mesh elements of phase field representing the pore space area for fluid flow.

Table 16: Simulation run times for incompressible Navier Stokes model using DIM at coarseness ratio of 10

Porosity	Number of mesh elements	Simulation run time (s)
0.67	10000	146.8406
0.6	10000	115.7824
0.493	10000	76.8592

Table 17: Simulation run times for incompressible Navier Stokes model using DIM at coarseness ratio of 6.67

Porosity	Number of mesh elements	Simulation run time (s)
0.67	22500	498.6665
0.6	22500	367.8449
0.493	22500	259.3919

5 CONCLUSIONS AND FUTURE WORKS

In summary, this work implemented diffuse interface method on structured quadrilateral meshes generated from volumetric images of porous media and determined characteristic coefficients of porous media from mass diffusion and incompressible Navier Stokes simulations. Specifically, binary images for three images with different porosities were generated to demonstrate the diffuse interface method. Phase fields were generated from binary images of porous media and projected onto structured quadrilateral meshes. Key parameters affecting the phase field and structured mesh were identified. Mass diffusion and incompressible Navier Stokes models were formulated with suitable initial and boundary conditions to best determine tortuosity, permeability, and inertial constants. Finite element method simulations for the mass diffusion and incompressible Navier Stokes models were performed on conformal meshes for the same images and provided reference solutions of tortuosity, permeability, and inertial constants.

Then firstly, diffuse interface method was applied for mass diffusion model to determine tortuosity and simulations were run at varying parameters identified for analysing diffuse interface method. The parameters which gave reasonable accuracy and low run time were determined and relative errors were found in tortuosity as compared to that from FEM on conformal meshes. Relative error in tortuosity less than 0.75% is achieved for all three images. Secondly, DIM was applied for incompressible Navier Stokes model to determine permeability and inertial constants. It was identified that Dirichlet boundary condition on the solid interface led to swelling of solid domain which severely affects the pressure gradient accuracy. To correct the solid domain sizing, isomorphic transformation was performed and expanse of solid domains in phase field was made equal to original image. Then, simulations were performed with varying parameters - porosity, coarseness ratio and DI width. Ideal parameters were found, and diffuse interface width was constrained. Finally, DIM INS simulations were performed at varying

inlet velocities at identified DI width and coarseness ratio to determine permeability and inertial constants from Forchheimer curves. The determined constants are presented with relative errors compared to reference converged conformal mesh solutions. Relative error in permeability less than 1% and relative error in inertial constant less than 3% is achieved for all three images.

There are some future works that could be done to expand on this work. These future works are listed as follows-

- Current implementation of incompressible Navier Stokes model using DIM is unreasonably slow compared to traditional finite element method. Optimized solvers for fluid flow need to be investigated and implemented for structured meshes to speed up the DIM simulations.
- Investigate GPU acceleration methods for simulations on structured meshes.
- This work determines the porous media property constants by simulations using FEM and DIM on artificially generated two dimensional binary images. Next step would be to conduct simulations on benchmark three dimensional volumetric images of porous media obtained from tomography.
- Tortuosity, permeability, and inertial constants obtained from conducting DIM simulations on benchmark three dimensional volumetric images of porous media can be compared to the experimental and simulation results existing in the literature in terms of accuracy and time performance.

6 BIBLIOGRAPHY

[1] B. L. Su, C. Sanchez, and X. Y. Yang, "Hierarchically Structured Porous Materials: From Nanoscience to Catalysis, Separation, Optics, Energy, and Life Science," *Hierarchically Struct. Porous Mater. From Nanosci. to Catal. Sep. Opt. Energy, Life Sci.*, Nov. 2011, doi: 10.1002/9783527639588.

[2] H. Li and M. C. Boufadel, "Long-term persistence of oil from the Exxon Valdez spill in two-layer beaches," *Nat. Geosci. 2010 32*, vol. 3, no. 2, pp. 96–99, Jan. 2010, doi: 10.1038/ngeo749.

[3] C. Noiriel, P. Gouze, and D. Bernard, "Investigation of porosity and permeability effects from microstructure changes during limestone dissolution," *Geophys. Res. Lett.*, vol. 31, no. 24, pp. 1–4, Dec. 2004, doi: 10.1029/2004GL021572.

[4] J. C. Eichelberger, C. R. Carrigan, H. R. Westrich, and R. H. Price, "Non-explosive silicic volcanism," *Nat. 1986 3236089*, vol. 323, no. 6089, pp. 598–602, 1986, doi: 10.1038/323598a0.

[5] V. Gitis, G. Rothenberg, V. Gitis, G. Rothenberg, A. A. Kiss, and D. Eisenberg, "Handbook of Porous Materials," vol. 4, Jan. 2021, doi: 10.1142/11909.

[6] N. Backeberg, F. Iacoviello, M. Rittner, T. M.-S. reports, and undefined 2017, "Quantifying the anisotropy and tortuosity of permeable pathways in clay-rich mudstones using models based on X-ray tomography," *nature.com*, Accessed: Aug. 28, 2021. [Online]. Available: https://www.nature.com/articles/s41598-017-14810-1.

[7] S. M. R. Niya and A. P. S. Selvadurai, "A Statistical Correlation Between Permeability, Porosity, Tortuosity and Conductance," *Transp. Porous Media 2017 1213*, vol. 121, no. 3, pp. 741–752, Dec. 2017, doi: 10.1007/S11242-017-0983-0.

[8] M. Oostrom *et al.*, "Pore-scale and continuum simulations of solute transport micromodel benchmark experiments," *Comput. Geosci.*, vol. 20, no. 4, pp. 857–879,

Jun. 2014, doi: 10.1007/S10596-014-9424-0.

[9]   J. Dompierre, M.-G. Vallet, Y. Bourgault, M. Fortin, and W. G. Habashi, "Anisotropic mesh adaptation: towards user-independent, mesh-independent and solver-independent CFD. Part III. Unstructured meshes," *Int. J. Numer. Methods Fluids*, vol. 39, no. 8, pp. 675–702, Jul. 2002, doi: 10.1002/FLD.357.

[10]   L. H. Nguyen, S. K. F. Stoter, M. Ruess, M. A. Sanchez Uribe, and D. Schillinger, "The diffuse Nitsche method: Dirichlet constraints on phase-field boundaries," *Int. J. Numer. Methods Eng.*, vol. 113, no. 4, pp. 601–633, Jan. 2018, doi: 10.1002/NME.5628.

[11]   E. J. Monte, J. Lowman, and N. M. Abukhdeir, "A diffuse interface method for simulation-based screening of heat transfer processes with complex geometries," Jan. 2021, Accessed: Aug. 30, 2021. [Online]. Available: https://arxiv.org/abs/2101.06824v1.

[12]   D. Schillinger *et al.*, "The non-symmetric Nitsche method for the parameter-free imposition of weak boundary and coupling conditions in immersed finite elements," *Comput. Methods Appl. Mech. Eng.*, 2016, doi: 10.1016/j.cma.2016.06.026.

[13]   S. K. F. Stoter, P. Müller, L. Cicalese, M. Tuveri, D. Schillinger, and T. J. R. Hughes, "A diffuse interface method for the Navier–Stokes/Darcy equations: Perfusion profile for a patient-specific human liver based on MRI scans," *Comput. Methods Appl. Mech. Eng.*, 2017, doi: 10.1016/j.cma.2017.04.002.

[14]   L. Nguyen, S. Stoter, T. Baum, … J. K.-… journal for numerical, and undefined 2017, "Phase-field boundary conditions for the voxel finite cell method: Surface-free stress analysis of CT-based bone structures," *Wiley Online Libr.*, vol. 33, no. 12, Dec. 2017, doi: 10.1002/cnm.2880.

[15]   S. Aland, F. Stenger, R. Müller, A. Deutsch, and A. Voigt, "A Phase Field Approach to Trabecular Bone Remodeling," *Front. Appl. Math. Stat.*, vol. 0, p. 12, May 2020, doi:

10.3389/FAMS.2020.00012.

[16]   E. Monte, "OpenCMP: An Open-Source Computational Multiphysics Package," 2021, Accessed: Aug. 30, 2021. [Online]. Available: https://uwspace.uwaterloo.ca/handle/10012/17239.

[17]   G. F. Pinder and W. G. Gray, "Essentials of Multiphase Flow and Transport in Porous Media," *Essentials Multiph. Flow Transp. Porous Media*, pp. 1–257, Feb. 2008, doi: 10.1002/9780470380802.

[18]   O. O. TAIWO *et al.*, "Comparison of three-dimensional analysis and stereological techniques for quantifying lithium-ion battery electrode microstructures," *J. Microsc.*, vol. 263, no. 3, pp. 280–292, Sep. 2016, doi: 10.1111/JMI.12389.

[19]   , S Torquato and , HW Haslach, "Random Heterogeneous Materials: Microstructure and Macroscopic Properties," *Appl. Mech. Rev.*, vol. 55, no. 4, pp. B62–B63, Jul. 2002, doi: 10.1115/1.1483342.

[20]   V. Patil *et al.*, "EXPERIMENTAL VERSUS COMPUTATIONAL METHODS IN THE STUDY OF FLOW IN POROUS MEDIA," 2014, Accessed: Sep. 02, 2021. [Online]. Available: http://asmedigitalcollection.asme.org/FEDSM/proceedings-pdf/FEDSM2014/46247/V01DT40A003/4454967/v01dt40a003-fedsm2014-21886.pdf.

[21]   A. Koponen, M. Kataja, and J. Timonen, "Permeability and effective porosity of porous media," *Phys. Rev. E - Stat. Physics, Plasmas, Fluids, Relat. Interdiscip. Top.*, vol. 56, no. 3, pp. 3319–3325, 1997, doi: 10.1103/PHYSREVE.56.3319.

[22]   A. Koponen, M. Kataja, and J. Timonen, "Tortuous flow in porous media," *Phys. Rev. E - Stat. Physics, Plasmas, Fluids, Relat. Interdiscip. Top.*, vol. 54, no. 1, pp. 406–410, 1996, doi: 10.1103/PHYSREVE.54.406.

[23]   P. Adler, *Porous media: geometry and transports*. 2013.

[24]   M. J. Blunt *et al.*, "Pore-scale imaging and modelling," *Adv. Water Resour.*, vol. 51,

pp. 197–216, Jan. 2013, doi: 10.1016/j.advwatres.2012.03.003.

[25] T. Bultreys, W. De Boever, V. C.-E.-S. Reviews, and undefined 2016, "Imaging and image-based fluid transport modeling at the pore scale in geological materials: A practical introduction to the current state-of-the-art," *Elsevier*, Accessed: Sep. 04, 2021. [Online]. Available: https://www.sciencedirect.com/science/article/pii/S0012825216300150?casa_t oken=34ctWTDM3vQAAAAA:3CHH8ugIv3exo8jI96qOEUzOPCWm8cLov1X922JD oego0E1PAdRuL-OUeeB8elvWJ5LgZjBIDw.

[26] M. Barrande, R. Bouchet, R. D.-A. chemistry, and undefined 2007, "Tortuosity of porous particles," *ACS Publ.*, vol. 79, no. 23, pp. 9115–9121, Dec. 2007, doi: 10.1021/ac071377r.

[27] B. Ghanbarian, A. Hunt, … R. E.-S. science society of, and undefined 2013, "Tortuosity in porous media: a critical review," *Wiley Online Libr.*, vol. 77, no. 5, pp. 1461–1477, Sep. 2013, doi: 10.2136/sssaj2012.0435.

[28] J. Fu, H. R. Thomas, and C. Li, "Tortuosity of porous media: Image analysis and physical simulation," *Earth-Science Reviews*, vol. 212. Elsevier B.V., p. 103439, Jan. 01, 2021, doi: 10.1016/j.earscirev.2020.103439.

[29] P. Adler, C. Jacquin, J. Q.-I. J. of Multiphase, and undefined 1990, "Flow in simulated porous media," *Elsevier*, Accessed: Sep. 04, 2021. [Online]. Available: https://www.sciencedirect.com/science/article/pii/030193229090025E.

[30] N. Srisutthiyakorn and G. M. Mavko, "What is the role of tortuosity in the Kozeny-Carman equation?," *Interpretation*, vol. 5, no. 1, pp. SB57–SB67, Jun. 2016, doi: 10.1190/INT-2016-0080.1.

[31] F. Masís-Meléndez, T. Deepagoda, … L. de J.-J. of, and undefined 2014, "Gas diffusion-derived tortuosity governs saturated hydraulic conductivity in sandy soils," *Elsevier*, Accessed: Sep. 04, 2021. [Online]. Available: https://www.sciencedirect.com/science/article/pii/S0022169414001711?casa_t

oken=OY-6-ZdwjvQAAAAA:Rv0InCosrKlHDPxJTiVwsEHJczybUIiCFPSm9vaLGt1Lm6fmLNcLG
o7YkmvxkZEpe2927ye3DA.

[32] D. Coelho, M. Shapiro, J. Thovert, P. A.-J. of colloid and, and undefined 1996, "Electroosmotic phenomena in porous media," *Elsevier*, Accessed: Sep. 04, 2021. [Online]. Available: https://www.sciencedirect.com/science/article/pii/S0021979796903690.

[33] D. Kehrwald, P. R. Shearing, N. P. Brandon, P. K. Sinha, and S. J. Harris, "Local Tortuosity Inhomogeneities in a Lithium Battery Composite Electrode," *J. Electrochem. Soc.*, vol. 158, no. 12, p. A1393, 2011, doi: 10.1149/2.079112JES/PDF.

[34] N. A. Zacharias, D. R. Nevers, C. Skelton, K. Knackstedt, D. E. Stephenson, and D. R. Wheeler, "Direct Measurements of Effective Ionic Transport in Porous Li-Ion Electrodes," *J. Electrochem. Soc.*, vol. 160, no. 2, pp. A306–A311, 2013, doi: 10.1149/2.062302JES/PDF.

[35] S. Prachayawarakorn, R. M.-C. today, and undefined 2007, "Effects of pore assembly architecture on catalyst particle tortuosity and reaction effectiveness," *Elsevier*, Accessed: Sep. 04, 2021. [Online]. Available: https://www.sciencedirect.com/science/article/pii/S0920586107003720?casa_t
oken=WZpcwdCO1gwAAAAA:Svv3xeiQvCpwYK8NY6R2Rl61v8vIefc5yjK9Ccuu0o
doRS9dGsrM07Yp9_BowBvFMUATdN7yqA.

[36] V. Karanikola, A. Corral, H. Jiang, … A. S.-J. of M., and undefined 2017, "Effects of membrane structure and operational variables on membrane distillation performance," *Elsevier*, Accessed: Sep. 04, 2021. [Online]. Available: https://www.sciencedirect.com/science/article/pii/S0376738816316258?casa_t
oken=dmxJWK2hrPoAAAAA:d4HU528b5KB6_LQoFX18Oh79YlJWhj4B7xAzffZm4
D1moApuFKRKTcf5uUxnQRKWr-aIBBFBKw.

[37] F. Bini, A. Pica, A. Marinozzi, F. M.-S. reports, and undefined 2019, "A 3D model of

the effect of tortuosity and constrictivity on the diffusion in mineralized collagen fibril," *nature.com*, Accessed: Sep. 04, 2021. [Online]. Available: https://www.nature.com/articles/s41598-019-39297-w.

[38] M. C.-G. Society, undefined London, undefined Special, and undefined 1997, "Tortuosity: a guide through the maze," *sp.lyellcollection.org*, Accessed: Sep. 04, 2021. [Online]. Available: https://sp.lyellcollection.org/content/122/1/299.short?casa_token=qmGwHkkO en4AAAAA:0UxRV87nxP9-OqX_e60nKMiuKj69Pjd7sF5njnku24kZCygsJWDiBJkexQx4H4zCwbaueOb6bwpOd w.

[39] R. Brodkey and H. Hershey, *Transport phenomena: a unified aprroach*. 2003.

[40] N. E.-C. engineering science and undefined 1989, "On tortuosity and the tortuosity factor in flow and diffusion through porous media," *Elsevier*, Accessed: Sep. 08, 2021. [Online]. Available: https://www.sciencedirect.com/science/article/pii/0009250989850535.

[41] B. Tjaden, J. Lane, P. Withers, R. Bradley, D. B.-S. S. Ionics, and undefined 2016, "The application of 3D imaging techniques, simulation and diffusion experiments to explore transport properties in porous oxygen transport membrane support," *Elsevier*, Accessed: Sep. 08, 2021. [Online]. Available: https://www.sciencedirect.com/science/article/pii/S0167273816000564?casa_t oken=V5P5HbplAkQAAAAA:_7Ppmk54z4C67vOieR2djzynHA-SzlyCCm_R1pZ_fBlwPrl6CnZvGNANA_3hwvPLGOpJZB5EyQ.

[42] H. Darcy, *Les fontaines publiques de la ville de Dijon: exposition et application...* 1856.

[43] M. M.-J. of A. Physics and undefined 1937, "The flow of fluids through porous media," *aip.scitation.org*, vol. 8, no. 4, p. 274, 1937, doi: 10.1063/1.1710292.

[44] P. Kundu, V. Kumar, I. M.-P. Technology, and undefined 2016, "Experimental and numerical investigation of fluid flow hydrodynamics in porous media:

Characterization of pre-Darcy, Darcy and non-Darcy flow regimes," *Elsevier*, Accessed: Sep. 09, 2021. [Online]. Available: https://www.sciencedirect.com/science/article/pii/S0032591016306209?casa_token=56LcN3csf-cAAAAA:oEP9fPQom84_Uo84a6WtMeG6MY-fSNQmz82pDyqsitN9RoXN8aG-vYwSCdssAhSogUGWIPPkCA.

[45]   P. F.-Z. V. Deutsch, undefined Ing., and undefined 1901, "Wasserbewegung durch boden," *ci.nii.ac.jp*, Accessed: Sep. 09, 2021. [Online]. Available: https://ci.nii.ac.jp/naid/10010395788/.

[46]   A. Nowamooz, G. Radilla, and M. Fourar, "Non-darcian two-phase flow in a transparent replica of a rough-walled rock fracture," *Water Resour. Res.*, vol. 45, no. 7, Jul. 2009, doi: 10.1029/2008WR007315.

[47]   M. Sukop, H. Huang, … P. A.-W. R., and undefined 2013, "Evaluation of permeability and non-Darcy flow in vuggy macroporous limestone aquifer samples with lattice Boltzmann methods," *Wiley Online Libr.*, vol. 49, no. 1, pp. 216–230, 2013, doi: 10.1029/2011WR011788.

[48]   E. Ghane, N. Fausey, L. B.-J. of Hydrology, and undefined 2014, "Non-Darcy flow of water through woodchip media," *Elsevier*, Accessed: Sep. 10, 2021. [Online]. Available: https://www.sciencedirect.com/science/article/pii/S0022169414007562?casa_token=K_eWDd1GlDcAAAAA:tBzmrlGk8gOgvDUggBSjWE93R3gvkVPEIFqAkPVNFr1R-LcGmEkD5yfwltmhftTap2CPf_y7yw.

[49]   Z. Zeng and R. Grigg, "A Criterion for Non-Darcy Flow in Porous Media," *Transp. Porous Media*, vol. 63, no. 1, pp. 57–69, Apr. 2006, doi: 10.1007/s11242-005-2720-3.

[50]   C. Cherubini, C. Giasi, N. P.-H. and E. System, and undefined 2012, "Bench scale laboratory tests to analyze non-linear flow in fractured media," *hess.copernicus.org*, vol. 16, pp. 2511–2522, 2012, doi: 10.5194/hess-16-2511-2012.

[51] I. I.- Washington and undefined 1986, "Handbook of hydraulic resistance," *ui.adsabs.harvard.edu*, Accessed: Sep. 10, 2021. [Online]. Available: https://ui.adsabs.harvard.edu/abs/1986wdch.book.....I/abstract.

[52] M. Piller, G. Schena, M. Nolich, … S. F.-T. in porous, and undefined 2009, "Analysis of hydraulic permeability in porous media: from high resolution X-ray tomography to direct numerical simulation," *Springer*, vol. 80, no. 1, pp. 57–78, 2009, doi: 10.1007/s11242-009-9338-9.

[53] R. O'Connor, J. F.-P. and C. of the Earth, P. A, and undefined 1999, "Microscale flow modelling in geologic materials," *Elsevier*, Accessed: Sep. 14, 2021. [Online]. Available: https://www.sciencedirect.com/science/article/pii/S1464189599000885.

[54] C. Geuzaine and J. F. Remacle, "Gmsh: A 3-D finite element mesh generator with built-in pre- and post-processing facilities," *Int. J. Numer. Methods Eng.*, vol. 79, no. 11, pp. 1309–1331, Sep. 2009, doi: 10.1002/NME.2579.

[55] "Avizo Software for materials research | Thermo Fisher Scientific - CA." https://www.thermofisher.com/ca/en/home/electron-microscopy/products/software-em-3d-vis/avizo-software.html (accessed Sep. 14, 2021).

[56] C. M.-C. Multiphysics, undefined Burlington, undefined MA, undefined accessed, and undefined 1998, "Introduction to comsol multiphysics®," *academia.edu*, Accessed: Sep. 14, 2021. [Online]. Available: https://www.academia.edu/download/34675355/01.Introduction_to_COMSOL_Multiphysics.pdf.

[57] J. Matsson, *An Introduction to ANSYS Fluent 2021*. 2021.

[58] S. Chen and G. D. Doolen, "Lattice boltzmann method for fluid flows," *Annu. Rev. Fluid Mech.*, vol. 30, pp. 329–364, 1998, doi: 10.1146/ANNUREV.FLUID.30.1.329.

[59] M. Goodarzi *et al.*, "Comparison of the finite volume and lattice boltzmann methods for solving natural convection heat transfer problems inside cavities and enclosures," *Abstr. Appl. Anal.*, vol. 2014, 2014, doi: 10.1155/2014/762184.

[60] A. Mohamad, *Lattice Boltzmann Method*. 2011.

[61] Y. Shi, T. Zhao, Z. G.-P. R. E, and undefined 2006, "Lattice Boltzmann method for incompressible flows with large pressure gradients," *APS*, vol. 73, no. 2, 2006, doi: 10.1103/PhysRevE.73.026704.

[62] R. Song, Y. Wang, J. Liu, M. Cui, and Y. Lei, "Comparative analysis on pore-scale permeability prediction on micro-CT images of rock using numerical and empirical approaches," *Energy Sci. Eng.*, vol. 7, no. 6, pp. 2842–2854, Dec. 2019, doi: 10.1002/ESE3.465.

[63] J. Nordström, J. Gong, … E. V. der W.-J. of C., and undefined 2009, "A stable and conservative high order multi-block method for the compressible Navier–Stokes equations," *Elsevier*, Accessed: Sep. 16, 2021. [Online]. Available: https://www.sciencedirect.com/science/article/pii/S0021999109004902?casa_token=36DBrmdrW60AAAAA:BIQOh9zV3ZVH00NKywg_bcKHUIcj6wRxZI7Sc-GVkmFi6PhDkkBUKZaj38-VG23D87PdCl7uWQ.

[64] S. Boivin, F. Cayré, J. H.-I. J. of T. Sciences, and undefined 2000, "A finite volume method to solve the Navier–Stokes equations for incompressible flows on unstructured meshes," *Elsevier*, vol. 39, pp. 806–825, 2000, doi: 10.1016/S1290-0729(00)00276-3.

[65] J. H. Ferziger and M. Perić, "Computational Methods for Fluid Dynamics," *Comput. Methods Fluid Dyn.*, 2002, doi: 10.1007/978-3-642-56026-2.

[66] L. Zhang, Z. C.-J. of A. Mathematics, and undefined 2011, "A stabilized mixed finite element method for single-phase compressible flow," *hindawi.com*, Accessed: Sep. 16, 2021. [Online]. Available: https://www.hindawi.com/journals/jam/2011/129724/.

[67]   R. Rice and D. Do, *Applied mathematics and modeling for chemical engineers*. 2012.

[68]   C. G.-P. of Fluids and   undefined 1995, "On the permeability of unidirectional fibrous media: a parallel computational approach," *aip.scitation.org*, vol. 7, no. 11, p. 2563, 1995, doi: 10.1063/1.868706.

[69]   M. Fourar, G. Radilla, R. Lenormand, C. M.-A. in Water, and undefined 2004, "On the non-linear behavior of a laminar single-phase flow through two and three-dimensional porous media," *Elsevier*, Accessed: Sep. 16, 2021. [Online]. Available: https://www.sciencedirect.com/science/article/pii/S030917080400048X?casa_token=bfy_D61B7fAAAAAA:1qDQ5ghqh4hx2C4Y9v-XX3SzkvSqcQDkA-9Tm36ldcp_EAMbZoFTSxzYY6iovdW0bdyE8lxJPw.

[70]   C. Li, S. Qiang, X. H.-J. of P. C. Series, and undefined 2020, "Advances in Automatic Hexahedral Meshing," *iopscience.iop.org*, vol. 1637, p. 12141, 2020, doi: 10.1088/1742-6596/1637/1/012141.

[71]   C. Armstrong, H. Fogg, C. Tierney, T. R.-P. Engineering, and undefined 2015, "Common themes in multi-block structured quad/hex mesh generation," *Elsevier*, Accessed: Sep.   16,   2021.   [Online].   Available: https://www.sciencedirect.com/science/article/pii/S1877705815032245.

[72]   J. Tu, G. Yeoh, and C. Liu, *Computational fluid dynamics: a practical approach*. 2018.

[73]   J. Schreiner, … C. S.-I. T. on, and   undefined 2006, "High-quality extraction of isosurfaces from regular and irregular grids," *ieeexplore.ieee.org*, Accessed: Sep. 16, 2021.   [Online].   Available: https://ieeexplore.ieee.org/abstract/document/4015483/?casa_token=0iarIUbTZ9gAAAAA:IduyL7yCCvExOZaUukTqV3ICcT1IuWmlkCT1LfH9OCHousnMlglaHhIN5r0I3Mrn2ibxamav.

[74]   J. Lindblad, "Surface area estimation of digitized planes using weighted local configurations," *Lect. Notes Comput. Sci. (including Subser. Lect. Notes Artif. Intell. Lect. Notes Bioinformatics)*, vol. 2886, pp. 348–357, 2003, doi: 10.1007/978-3-540-

39966-7_33.

[75]   J. Gostick, Z. Khan, T. Tranter, ... M. K.-J. of O., and undefined 2019, "PoreSpy: A python toolkit for quantitative analysis of porous media images," *joss.theoj.org*, 2019, doi: 10.21105/joss.01296.

[76]   Schöberl Joachim, "Netgen/NGSolve." https://ngsolve.org/ (accessed Sep. 17, 2021).

[77]   "edt · PyPI." https://pypi.org/project/edt/ (accessed Sep. 18, 2021).

[78]   P. Virtanen *et al.*, "SciPy 1.0: fundamental algorithms for scientific computing in Python.," *Nat. Methods*, pp. 1–12, Feb. 2020, doi: 10.1038/s41592-019-0686-2.

[79]   J. Ahrens, B. Geveci, C. L.-T. visualization handbook, and undefined 2005, "Paraview: An end-user tool for large data visualization," *datascience.dsscale.org*, Accessed: Sep. 20, 2021. [Online]. Available: https://datascience.dsscale.org/wp-content/uploads/2016/06/ParaView.pdf.

[80]   K. N. Moutsopoulos, I. N. E. Papaspyros, and V. A. Tsihrintzis, "Experimental investigation of inertial flow processes in porous media," *J. Hydrol.*, vol. 374, no. 3–4, pp. 242–254, Aug. 2009, doi: 10.1016/J.JHYDROL.2009.06.015.